Large-scale modes of turbulent channel flow: Transport and structure

By Z. LIU [1,2], R. J. ADRIAN[1]
AND T. J. HANRATTY[2]

[1] Laboratory for Turbulence and Complex Flow,
Department of Theoretical and Applied Mechanics,
[2]Department of Chemical Engineering,
University of Illinois, Urbana, Illinois 61801, USA

Turbulent flow in a rectangular channel flow is investigated to determine the scale and pattern of the eddies that contribute most to the total turbulent kinetic energy and the Reynolds shear stress. Instantaneous, two-dimensional particle image velocimetry measurements in the streamwise-wall-normal plane at Reynolds numbers Re_h= 5,378 and 29,935 are used to form two-point spatial correlation functions, from which the proper orthogonal modes are determined. Large-scale motions represented by a small set of lower-order eigenmodes contain a large fraction of the kinetic energy of the streamwise velocity component, and a small fraction of the kinetic energy of the wall-normal velocities, consistent with Townsend (1958). Surprisingly, the set of large-scale modes that contain fifty-per cent of the total turbulent kinetic energy in the channel, also contains seventy-five per cent of the total Reynolds shear stress in the outer region. Thus, the large-scale motions dominate turbulent transport in all parts of the channel except the buffer layer. The flow structures are extracted from individual realizations of the flow field by using the dominant eigenfunctions as a low-pass filter. In the streamwise wall-normal plane their pattern often consists of an inclined region of second quadrant vectors separated from an upstream region of fourth quadrant vectors by a stagnation point/shear layer. The inclined Q4/shear/Q2 region of the largest motions extends beyond the centerline of the channel and lies under a region of fluid that rotates about the spanwise direction. Reynolds number similarity of the large structures is demonstrated, approximately, by comparing the two-dimensional correlation coefficients and the eigenvalues of the different modes at the two Reynolds numbers.

1. Introduction

It is implicit in the velocity defect law and other statements of outer flow similarity for turbulent flow over walls that large-scale motions scaling with the outer length-scale exist in these flows. As in the inner wall-layer, these motions are coherent in the sense that they have characteristic flow patterns that persist over times long enough to contribute significantly to the time average character of the flow. Perhaps the best known large-scale motions are the bulges of the turbulent boundary layer which travel at approximately eighty per cent of the free-stream velocity and are about two-boundary layer thickness long and 1-2 boundary layer thickness wide (Kovasznay, Kibens & Blackwelder 1970, Murlis, Tsai & Bradshaw 1982). The low-speed puffs observed by Wygnanski & Champagne (1973) are another well-known type of large-scale motion that occurs in pipe flow, albeit only at sufficiently low Reynolds numbers and/or sufficiently smooth entry conditions. Large-scale motions in the form of two-dimensional roll-cells oriented with their rotation axis in the streamwise direction and spanning the width of the

flow have been observed in plane turbulent Couette flow; however, in this case the rolls cells appear to be steady and may therefore be better interpreted as secondary flow instabilities of the mean flow (Papavassiliou & Hanratty, 1997; Lee & Kim 1991).

Although the low-speed streaks that occur in the buffer layer of wall turbulence have very long dimensions in the streamwise x-direction, their spanwise and wall-normal scales are small, of the order of 100 viscous wall units (Kline *et al.* 1967, Robinson 1991). Therefore, at elevated Reynolds numbers, where the ratio of the outer length-scale to the inner viscous length-scale is large, near-wall streaks are very thin, and the large-scale motions are distinguished from them by their much larger extent in the wall-normal y-direction and the spanwise z-direction. In the present work, which deals with data in the x-y plane, 'large-scale' will denote motions that are large in both the x- and y- directions.

Townsend (1958) and Grant (1958) both observed that the long tail on the streamwise correlation function of the streamwise velocity implied that large-scale motions contribute significantly to the streamwise kinetic energy. Townsend (1958, 1976) argued that long extent in the x-direction implied small values of the v-component of velocity, and hence small contributions to the Reynolds shear stress, even though the contribution to the kinetic energy of u is large. He termed the large eddies close to the wall "inactive", and focused attention on the "main" turbulence eddies which are those with length scales in the inertial range. Several experimental investigations provide spectral data that can be interpreted to support Townsend's view that large-scale motions contain a substantial fraction of the streamwise kinetic energy, c.f. Lekakis (1988), for example. A few studies (Naguib &Wark 1992; Adrian & Lekakis 1991) have reported direct observations of this effect.

However, a question exists about the degree to which large-scale motions contribute to the Reynolds shear stress. Using Lekakis' (1988) correlation data, stochastic estimates of $\langle u(t+\tau), v(t+\tau) | u(t), v(t) \rangle$ indicate that following events in which the Reynolds shear stress $u(t)v(t)$ has large values in either the second quadrant (Q2) or fourth quadrant (Q4), there is a rapid transient decay of $\langle u(t+\tau), v(t+\tau) | u(t), v(t) \rangle$ followed by a long time during which the velocity disturbance decays slowly (Adrian & Lekakis 1991). Thus, most of the time that the flow vector spends in the Q2 or Q4 quadrants is due to large time-scale events, i.e. long length-scale motions.

One-dimensional analysis of the type provided by spectral analysis of hot-wire or LDV signal is deficient in that it cannot identify the scale of a structure in anything but the mean flow direction. In particular, one cannot distinguish between the contributions from long, thin structures such as near-wall streaks, and the long, thick structures that might occur in the outer region of wall turbulence. Two- or three-dimensional analysis must be used, and for this purpose visualization of two-dimensional PIV data permits some insights into the large-scale motions in boundary layers (c.f. Adrian, *et al.* 1998, 1999, for example). The present work is motivated by PIV (particle image velocimetry) visualizations in channel flow of large Reynolds stresses associated with large-scale motions with sizes that are, approximately, independent of Reynolds number. On average, they have dimensions of about 1/4 of the channel height in the wall-normal direction and more than two channel heights in the streamwise direction. Gaussian and spectral sharp-cut filters were used in an attempt to characterize these motions (Hanratty *et al.*, 1993). These had a number of disadvantages in that they could not easily accommodate changes of scale in the normal direction and a certain amount personal judgment entered into the analysis.

Proper orthogonal decomposition (POD) is the correct quantitative way of representing the distribution of energy among various scales in each direction when the flow is statistically inhomogeneous in one or more directions. It decomposes the vector signal into modes having

scale in each direction and allows direct evaluation of the contribution that each mode makes to energy and Reynolds-stress. Therefore, the POD method is used here to provide a precise and well-defined evaluation of the scales of motion contributing to both the energy and stress-producing events.

A number of previous investigators have used this approach to characterize the structure of turbulence. Bakewell & Lumley (1967) obtained the most energetic eddy structure in the wall region ($y^+ < 40$, where $y^+ = yu_\tau/\nu$ is the usual inner layer coordinate made non-dimensional by the viscous length scale based on the friction velocity u_τ and the kinematic viscosity ν) in a turbulent pipe flow at $Re_D = 8{,}700$. They measured only the $Re_{11}(r_x)$ component of the correlation tensor, and obtained the other components by using a mixing-length assumption and conservation of mass. Only one eigenmode was calculated. The assumption of zero phase was used to reconstruct a typical eddy, which carried over 90% of the total streamwise turbulent intensity. They concluded that the dominant structure in the wall region consists of counter-rotating eddy pairs of elongated extent that are tilted in the upstream direction.

Herzog (1986) measured four components of the correlation tensor R_{ij}, $i, j = 1, 3$, at six points in the wall-normal and circumferential directions and at seven points in the streamwise direction in a pipe flow at $Re_D = 8{,}750$ ($u_\tau h/\nu = 531$). The rest of the components of the tensor were reconstructed from continuity. The decomposition domain, $0 \le y^+ \le 40$, was far too small to encompass the large-scale structures we are interested in here, but the results they found for the buffer layer structure are of interest for later comparison. The maximum eigenvalue was found to be dominant for a wave number of $k_1\nu/u_\tau = 0$, $n = 1$ and $k_3\nu/u_\tau = 0.0035$. The first contained 60% of the streamwise turbulent intensity, and the first three eigenmodes contained almost all of the total energy. A shot noise expansion was used to determine the phase of a typical eddy. With a zero-phase reconstruction, a typical eddy was found to be a pair of counter-rotating vortices whose centers were 30 – 40 above the wall, 65 viscous length scales apart, and 400 viscous length scales in extent. They were tilted at 5^0 to the wall.

Moin & Moser (1989) applied POD to one (y), two (y-z) and three-dimensional decompositions of turbulent channel flow at a low Reynolds number $Re_h = 2{,}800$ ($Re_\tau = u_\tau h/\nu = 180$). The two-point velocity correlation tensor $R_{ij}(r_x, y, y', r_z)$, $i, j = 1, 2, 3$, were computed using DNS data. Domains of $0 < y^+ < 40$, $140 < y^+ < 180$ and $0 < y^+ < 180$ were used. A shot noise expansion was used in an effort to determine the phase. The resulting zero-phase characteristic eddy, which contributed as much as 76% of the kinetic energy, was found to consist of a narrow ejection straddled by a pair of weak streamwise counter-rotating vortices with a streamwise extent of less than 100^+. They are inclined at 10° near the wall and as much as 60°, farther away from the wall. Sirovich, *et al.* (1990, 1991) also used DNS data to calculate correlation and spectral tensors at low Reynolds numbers $u_b h/\nu = 1{,}200$, $1{,}800$ ($u_\tau h/\nu = 80, 125$). They considered only the $Re_h = 1{,}800$ study to be fully developed. The decomposition domain was the full channel height. A three-dimensional decomposition was performed; sixteen modes with wave numbers ($k_1 = 0 - 1$, $n = 1 - 2$, $k_3 = 0 - 3$) were found to account for 60% of the total energy in the flow, where k_1 and k_3 denote the numbers of full waves in the streamwise and spanwise directions and n is the eigenmode order in the wall-normal direction. The most energetic mode with $k_1 \neq 0$ for the two cases is $k_1 = 1$, $n = 1$, $k_3 = 3$.

All of the foregoing POD results are at low Reynolds number, and the behavior at high Reynolds number is less well understood. Chambers, *et al.* (1988) used Burgers' equation with random forcing to create a stationary, spatially inhomogeneous flow structure possessing the characteristics of a two-scale boundary layer at the endpoints of the unit interval. The POD

eigenfunctions in the inhomogeneous spatial variable were found to be similar, over a range of Reynolds numbers, when they are scaled with outer variables. They suggested that the POD of real turbulence might also obey such a generalized law of Reynolds number similarity.

Liu, *et al.* (1994, 1995) obtained the POD from measurements in the x-y plane of channel flow at the same Reynolds numbers reported here. The structure of the 1-D POD eigenfunctions consisted of a thin layer close to the wall, of order of the buffer layer thickness, in which the modes decreased rapidly to zero at the wall, and an outer region in which the structure of the modes was essentially independent of the Reynolds number. The eigenvalue spectra of the channel flow were shown to correlate well with those of a boundary layer flow (Lu & Smith 1991), supporting the notion that outer layer similarity applies to at least two types of wall turbulence. Outer layer Reynolds similarity of the POD is a strong form of the similarity usually found from the mean velocity. Its validity is based on data at a relatively low Reynolds number; so further work is needed to test its generality for all Reynolds numbers. Even so, outer similarity of the POD modes suggests that the form of the large-scale motions and the amounts they contribute to energy and Reynolds stress may also be independent of Reynolds number.

This paper examines the significance and structure of large-scale motions by considering turbulent flow in a channel. Particle-image velocimetry (Adrian, 1991) is used to capture, at different instances of time, the spatial variation of the two components of the velocity in a plane that is perpendicular to the wall and oriented in the flow direction (x-y). Two-dimensional spatial correlations are determined by averaging a number of realizations of the flow. These correlations are analyzed by proper orthogonal decomposition to arrive at a representation of the flow field as the sum of 5,346 two-dimensional orthogonal eigenfunctions.

Two Reynolds numbers were studied $Re_h = U_b h/\nu$ = 5,378 and 29,935 (or $Re_\tau = u_\tau h/\nu$ = 315 and 1,414, where U_b is the bulk velocity, and h is the half-height of the channel). These conditions are identical to those in Liu *et al.* (1991, 1994). Because of limitations in the spatial resolution of PIV close to the wall, all of these studies focus on the outer flow, for which the appropriate length scale is normally assumed to be independent of Reynolds number and proportional to the channel height.

By virtue of the orthogonality property, the contributions of each POD mode to the total Reynolds stress and to the total energy are additive. In this way, it is shown that most of the Reynolds stress is carried by a small number eigenmodes representing large-scale events. Each instantaneous measurement of the velocity field can be represented by a linear combination of the eigenfunctions. By summing the small number of eigenfunctions that contain most of the Reynolds stress, the coherent structure of interest, in an individual realization of the field, can be captured. Since these are the large-scale motions, this procedure represents a low-pass filtration. Similarity is explored by comparing, at the two Reynolds numbers, the two-dimensional spatial correlations and the fractional contributions of the different eigenmodes to the Reynolds stress and to the kinetic energy.

The research described in this paper and in Liu *et al.* (1994, 1995) differs from previous POD studies in that it uses laboratory measurements at a much larger number of points and that it studies larger Reynolds numbers. The interpretation of the eigenfunctions is also somewhat different from previous studies in that no attempt is made to use the eigenfunctions to represent a characteristic eddy. Instead, the structure of the large eddies is found by using the eigenfunctions as a low-pass filter that extracts the motions that are large contributors to the Reynolds stress (Liu *et al.* 1995).

2. Experimental Procedures

Physical lengths made dimensionless by the viscous length scale are denoted by the usual notation (x^+, y^+, z^+), but fluctuating velocity components normalized by the wall-friction velocity u_τ are denoted by (u, v, w) = (u_1, u_2, u_3), the superscript "+" being omitted to avoid clutter in the POD equations. The two-dimensional channel flow facility contained water, and its rectangular cross-section was 609.6 mm wide by $2h$ = 48.75 mm high. The channel and the single-lens, photographic particle image velocimeter used to measure velocity in this study have been described in detail in Liu, *et al.* (1991, 1994). Documentation of the flow in this channel based on laser Doppler velocimeter measurements at Reynolds numbers ranging from 2,778 to 30,000 can also be found in studies by Niederschulte, *et al.* (1990), Warholic (1997) and Guenther, *et al.* (1998). All of the experimental measurements of conventional turbulence statistics through fourth-order are consistent with generally accepted behavior of channel flow, as found in the experiments of other investigators, and in direct numerical simulations.

The PIV provided instantaneous measurements of (u, v) on an x-y plane that extended from $y = 0$, to $y = 2h$, and the length of the data domain in the streamwise direction was L_x = 78 mm = $3.2h$, as determined by the field-of-view of the PIV camera. More than 5000 vectors were calculated from each PIV photograph, and an ensemble of 60 - 80 photographs was obtained at each Reynolds number. The flow parameters are listed in Table 1. The measurement volume used to obtain a vector during interrogation was (Δx_0, Δy_0, Δz_0) = (1.6 mm, 0.8 mm, 0.8 mm). These dimensions normalized with viscous wall units and with the outer length scale, h, are listed in Table 2. The spacing between vectors was 1.2 mm in the x-direction and 0.6 mm in the y-direction. The measurements closest to the wall were at y^+ = 5.16 and 23.2 for the two Reynolds numbers, respectively. At the lower Reynolds number the spatial resolution is comparable to that achieved in direct numerical simulations, but at the higher Reynolds number each measured vector represents an average over a significant range of small scales. For example, the resolution in the y-direction Δy_0^+ = 46.5 was clearly inadequate to resolve the buffer layer. However its size relative to the outer scale, $\Delta y/h$ = 0.032, was small enough to allow the evaluation of 15 POD modes in the y-direction. Thus, the range of validity of our measurements of the POD modes and eigenvalue spectra is restricted to the lower orders that are adequately resolved by the measurements.

Table 1: Flow parameters

$U_b h/\nu$	$u_\tau h/\nu = h^+$	L_x^+	U_b(mm/s)	u_τ(mm/s)	ν/u_τ(mm)
5,378	315	1,008	212	12.4	0.0775
29,935	1,414	4,520	1,074	50.7	0.0172

Table 2: The measurement volume in the PIV experiments

$U_b h/\nu$	Δx_o^+	Δy_o^+	Δz_o^+	$\Delta x_o/h$	$\Delta y_o/h$	$\Delta z_o/h$
5,378	20.6	10.3	10.3	0.065	0.032	0.032
29,935	93.0	46.5	46.5	0.065	0.032	0.032

3. Proper Orthogonal Decomposition

Proper orthogonal decomposition of the experimental channel flow data is performed on the domain ($0 \le x \le 1$, $0 \le y \le 1$) where x denotes the streamwise coordinate normalized by L_x = 78mm = $3.2h$, and y denotes the wall-normal coordinate normalized by $2h$. It is well known

(Lumley 1970) that the eigenfunctions of the POD are trigonometric in a statistically homogeneous direction such as the streamwise direction in the channel. Therefore, on ($0 \le x \le 1$, $0 \le y \le 1$) we can represent the i^{th} component of the velocity, $u_i(x, y)$ by the Fourier series

$$u_i(x,y) = \sum_k \hat{u}_i(k,y) e^{j2\pi kx}, \tag{1}$$

where the Fourier coefficient $\hat{u}_i(k,y)$

$$\hat{u}_i(k,y) = \int_0^1 u_i(x,y) e^{-j2\pi kx} dx, \tag{2}$$

is a random function of the inhomogeneous direction y with parameter k. The two-dimensional proper orthogonal decomposition is completed by expanding $\hat{u}_i(k,y)$ in a Karhunen-Loève expansion

$$\hat{u}_i(k,y) = \sum_n a^{(k,n)} \phi_i^{(k,n)}(y), \tag{3}$$

wherein the basis functions $\phi_i^{(k,n)}(y)$ are orthogonal,

$$\int_0^1 \phi_i^{(k,n)}(y)\, \phi_i^{(k,n')*}(y) dy = \delta_{nn'}. \tag{4}$$

The Fourier coefficients are given by

$$a^{(k,n)} = \int_0^1 \phi_i^{(k,n)*}(y)\, \hat{u}_i(\mathrm{k},y) dy. \tag{5}$$

Requiring the Fourier coefficients to be statistically orthogonal,

$$\langle a^{(k,n)} a^{(k',n')*} \rangle = \lambda^{(k,n)}\, \delta_{nn'}\, \delta_{kk'}, \tag{6}$$

and requiring the basis functions $\phi_i^{(k,n)}(y)$ to have the property that the partial sums of (3) converge faster than the partial sums of any other set of orthogonal functions results in the following integral equation for $\phi_i^{(k,n)}(y)$:

$$\int_0^1 K_{ij}^{(k)}(y,y')\, \phi_j^{(k,n)}(y')\, \mathrm{d}y' = \lambda^{(k,n)}\, \phi_i^{(k,n)}(y), \qquad i,j = 1,2 \tag{7}$$

where

$$K_{ij}^{(k)}(y,y') = \langle \hat{u}_i(k,y)\, \hat{u}_i^*(k,y') \rangle. \tag{8}$$

The kernel $K_{ij}^{(k)}(y,y')$ is related to the two-point spatial correlation tensor

$$R_{ij}(r_x, y, y') = \langle u_i(x,y)\, u_j^*(x + r_x, y') \rangle \tag{9}$$

by

$$K_{ij}^{(k)}(y,y') = \int_0^1 (1 - r_x) R_{ij}(r_x, y, y') e^{j2\pi k r_x} dr_x . \tag{10}$$

The spatial correlation tensor is calculated from the PIV data by forming the product of velocity components, ensemble averaging over the ensemble of experimental fields, and line averaging over the x-direction. The ensemble average for a given (r_x, y, y') extends only over those realizations that have valid vector data at those points. The effect of missing data is accounted for by dividing by the number of valid data in the ensemble at each point. The separations between the two points in the correlation functions are in the wall-normal and streamwise directions. Separations in spanwise direction and time-lags are not considered.

Combining the foregoing equations gives

$$u_i(x,y) = \sum_k \sum_n a^{(k,n)} \psi_i^{(k,n)}(x,y), \tag{11}$$

where

$$\psi_i^{(k,n)}(x,y) = \phi_i^{(k,n)}(y)\, e^{j2\pi kx} \tag{12}$$

is the two-dimensionally orthogonal eigenfunction of the complete POD expansion, which satisfies the orthogonality condition,

$$\int_0^1 \psi_i^{(k,n)}(x,y)\ \psi_i^{(k,n)*}(x,y)\, dxdy = \delta_{nn'}\ \delta_{kk'} . \tag{13}$$

The eigenfunction of the i^{th} velocity component $\phi_I^{(k,n)}(y)$ is a Fourier mode of order k in the streamwise direction and order n in the wall-normal direction. The order k is associated with a wavelength L_x/k. The principal usefulness of the POD is that it also associates a length scale in the y-direction with the modal order n, but since the statistical inhomogeneity in this direction implies varying length scale, the modal order n cannot be related to a single length. Rather, the structure of the eigenfunction itself defines the length scales for each mode. It has been shown that the modes approach trigonometric form as the modal order increases (Sung & Adrian 1994, Moser 1994) and the mode becomes associated with a length scale $2h/n$ for large n. Thus, POD decomposition makes it possible to evaluate the contribution of structures on the basis of their size in both the streamwise and the wall-normal directions, i.e. structures that are, for example, long in x, but narrow in y, or structures that are large in both x and y.

The contributions of structures of various sizes can be evaluated quantitatively by summing the contributions from the various modes. This is possible because the modes are statistically uncorrelated. For the turbulent kinetic energy,

$$E = \int_0^1 \langle u_i(x,y)\, u_i^*(x,y) \rangle dy = \sum_k \sum_n \lambda^{(k,n)} . \tag{14}$$

For the turbulent Reynolds stress

$$\langle u_i(x,y)\ u_j^*(x,y)\rangle = \sum_k \sum_n \lambda^{(k,n)}\ \phi_i^{(k,n)}(y)\ \phi_j^{(k,n)*}(y)\ , \tag{15}$$

and

$$\int_0^1 \langle u_i(x,y)\ u_j^*(x,y)\rangle dy = \sum_k \sum_n \lambda^{(k,n)} \int_0^1 \phi_i^{(k,n)}(y)\ \phi_j^{(k,n)*}(y) dy\ . \tag{16}$$

The mode order k equals the number of sinusoidal wavelengths in the domain L_x. It is related to streamwise wavenumber by $k_x = (2\pi/L_x)k$. Superscript n represents the mode order in the inhomogeneous wall-normal direction. In a one-dimensional decomposition (Liu *et al.*, 1994) n is the number of zero-crossings of the eigenfunctions. However, in two- or three-dimensional decompositions the interpretation is more complicated because the eigenfunctions are complex. Term $\lambda^{(k,n)}$ is the eigenvalue of the mode with orders n and k.

4. Distribution and structure of energy and transport

4.1 The two-point correlation functions

Contours of the two-point auto-correlation coefficients with separations in both y- and x-directions, $R_{ij}(r_x, y, y')/\sigma_i(y)\sigma_j(y')$, $i, j = u, v$, are plotted in Fig. 1 for $Re_h = 5{,}378$ and in Fig. 2 for $Re_h = 29{,}935$. Here σ_i denotes the root-mean-square value of the fluctuation of the i^{th}-component of velocity. The auto-correlation functions are given for the fixed point, y, located at different distances from the wall: $y/h = 0.065$, 0.237, 0.508, and 1.0. These correspond to $y^+ =$ 20.5, 75, 160 and 315 for the low Reynolds number, and $y^+ = 92$, 335, 718, and 1,414 for the high Reynolds number. Statistical sampling error of the two-dimensional correlation functions is estimated to be ±10% of the peak correlation value. Corresponding contour plots of the cross-correlations $(i,j) = (1, 2)$ and $(2, 1)$ are available from the editorial office.

In the outer region the correlation contours for the two Reynolds numbers are qualitatively similar when the separations of the two points in both the x- and y-directions are scaled with h, supporting the notion that the structure of large-scale motions exhibits Reynolds number similarity, (Townsend, 1976). However, there are some differences, one being a tendency for the highly correlated regions (say 0.8 or higher) of the higher Reynolds number data to be smaller than the highly correlated region of the lower Reynolds number data. This effect is expected because the ratio between the Taylor microscale and the integral length scale decreases with increasing Reynolds number. A more fundamental Reynolds number effect has to do with the streamwise extent of the streamwise velocity correlation. Relative to the lower Reynolds number case, the length of the correlated region at the higher Reynolds number is longer close to the wall (compare Fig. 2(a1) and (a2) to Fig. 1(a1) and (a2)) and shorter farther away from the wall (compare Fig. 2(a3) and (a4) to Fig. 1(a3) and (a4)). The longer extent of the high Reynolds number correlation closer to the wall may reflect correlation between the near-wall eddies and other, larger scale eddies.

Auto-correlations of the streamwise component for fixed points not on the centerline exhibit a characteristic shape that is elongated in the streamwise direction and inclined at a shallow angle to the wall. The average angle is 6° and 8° at the lower and higher Reynolds numbers, respectively. Symmetry forces the inclination to vanish when the fixed point is at the centerline of the channel. The length and height of the region of high positive correlation grow with increasing distance of the fixed point from the wall. The streamwise length attains a value in

(a1)

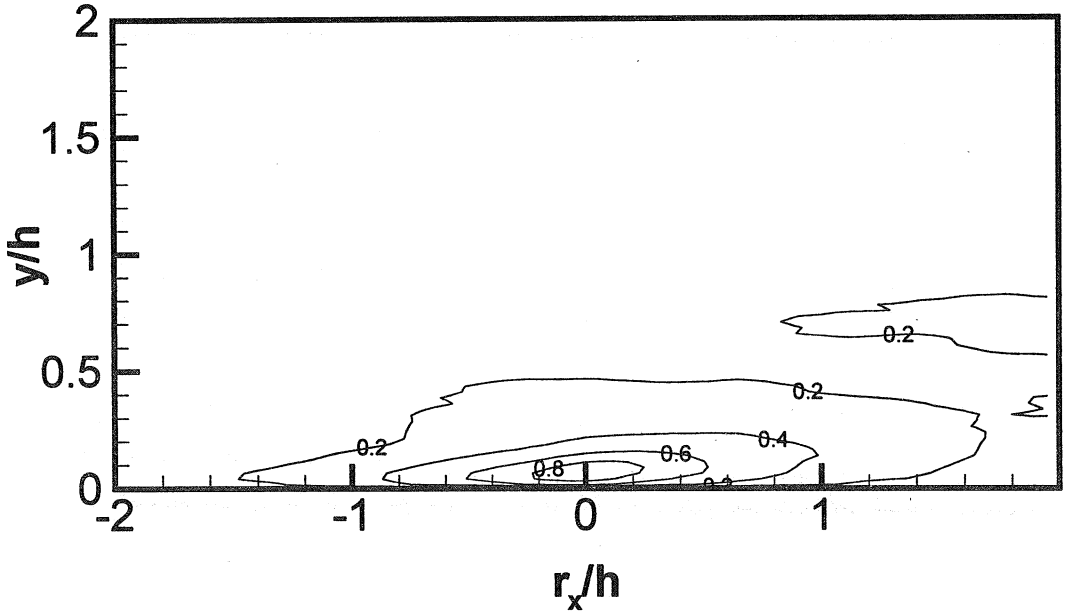
2
1.5
1
0.5
0
y/h
-2
-1
0
1
r_x/h
0.2
0.2
0.4
0.6
0.8

(a2)

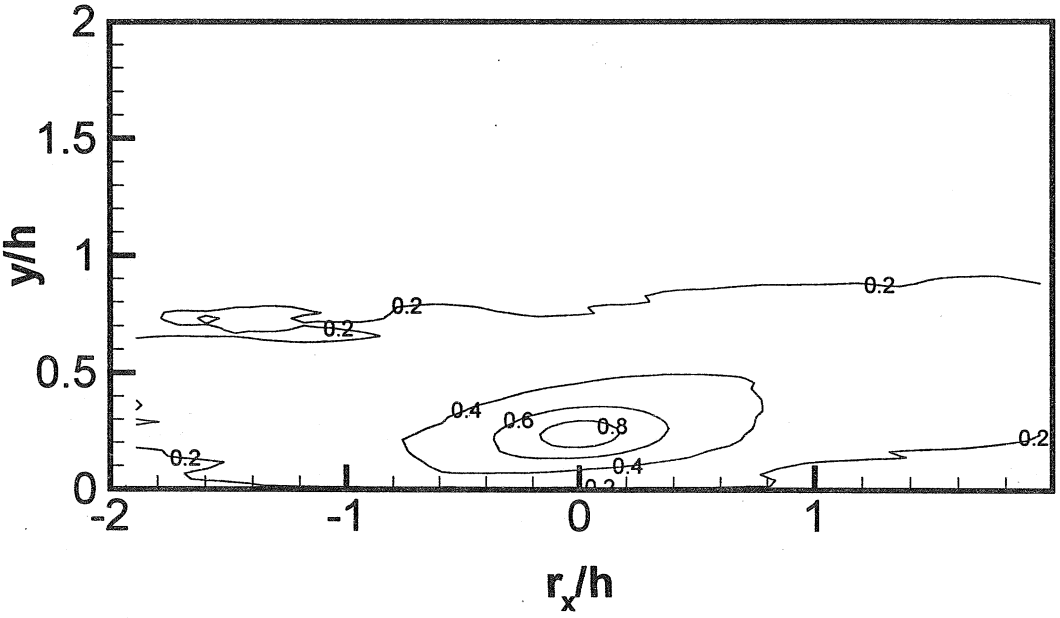
2
1.5
1
0.5
0
y/h
-2
-1
0
1
r_x/h
0.2
0.2
0.2
0.2
0.4
0.6
0.8
0.4
0.2

(a3)

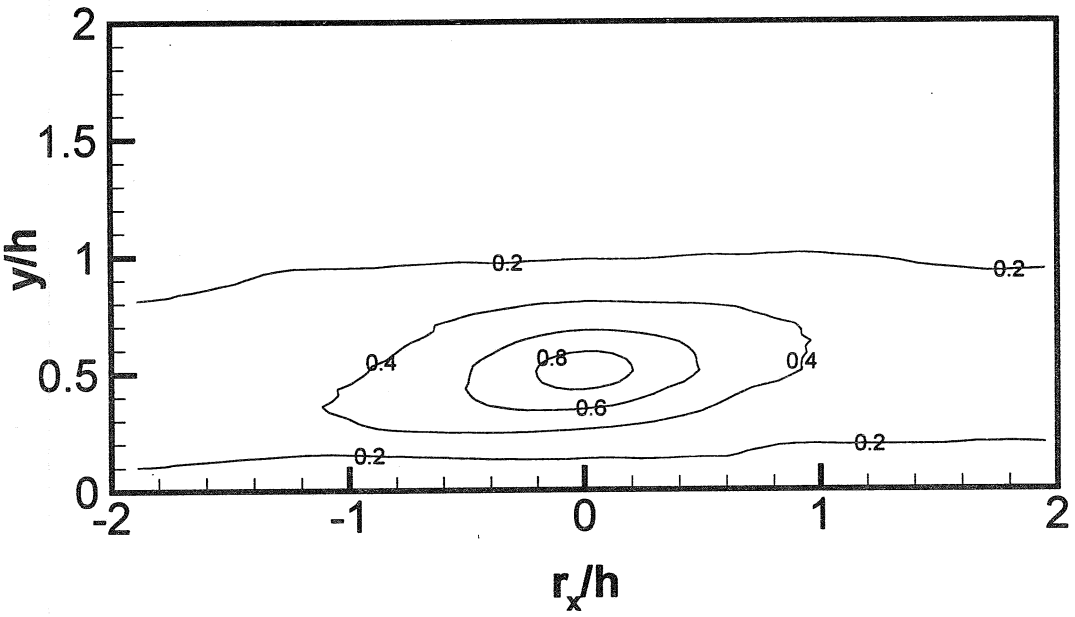
2
1.5
1
0.5
0
y/h
-2
-1
0
1
2
r_x/h
0.2
0.2
0.4
0.8
0.4
0.6
0.2
0.2

(a4)

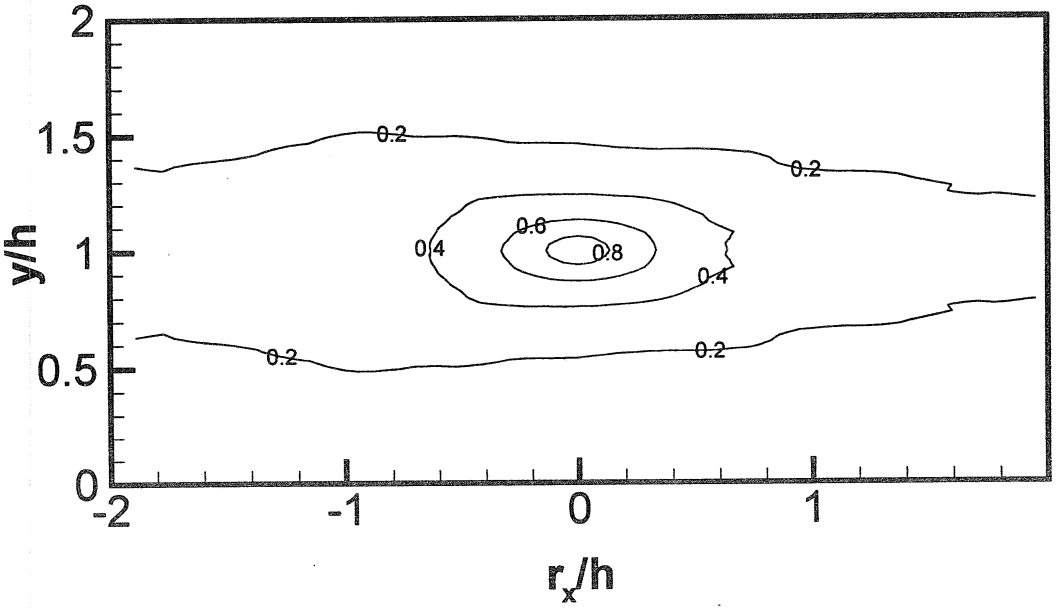
2
1.5
1
0.5
0
y/h
-2
-1
0
1
r_x/h
0.2
0.2
0.6
0.4
0.8
0.4
0.2
0.2

(b1)

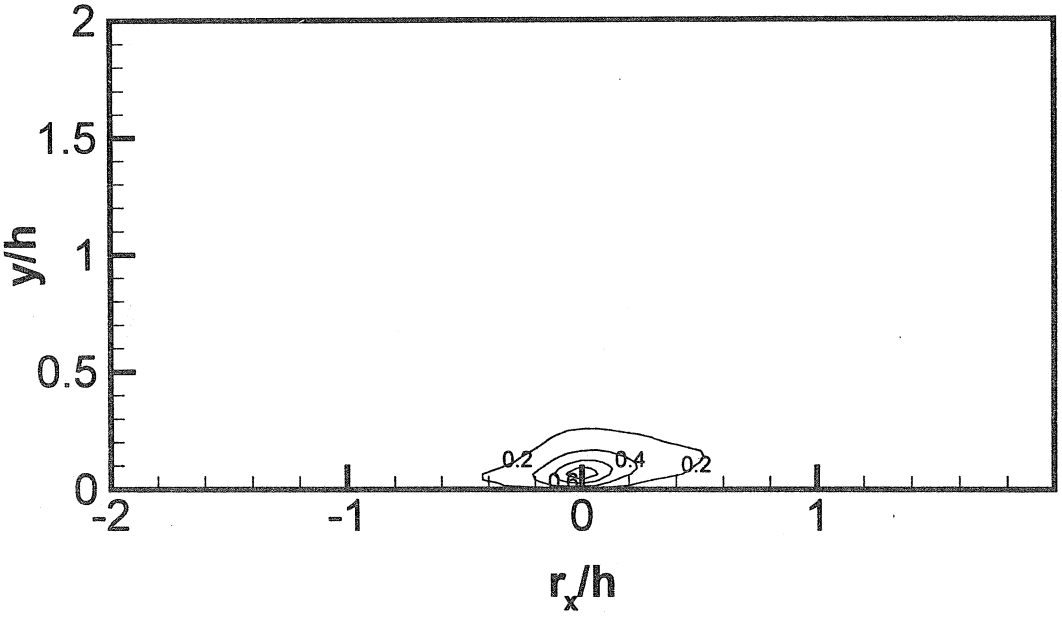
2
1.5
1
0.5
0
y/h
-2
-1
0
1
r_x/h
0.2
0.4
0.2

(b2)

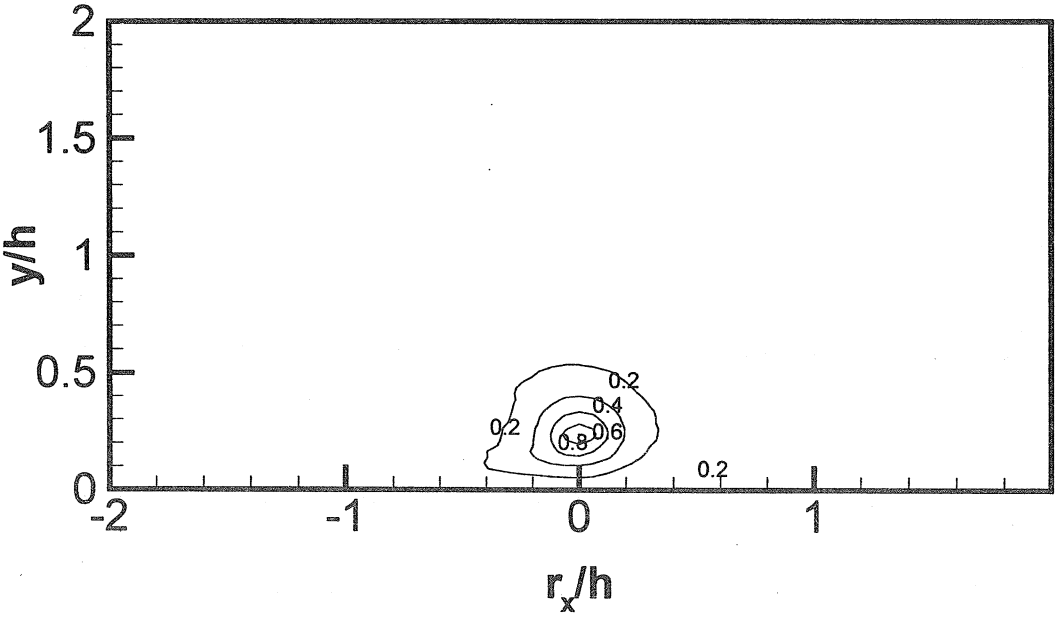
2
1.5
1
0.5
0
y/h
-2
-1
0
1
r_x/h
0.2
0.4
0.2
0.6
0.8
0.2

(b3)

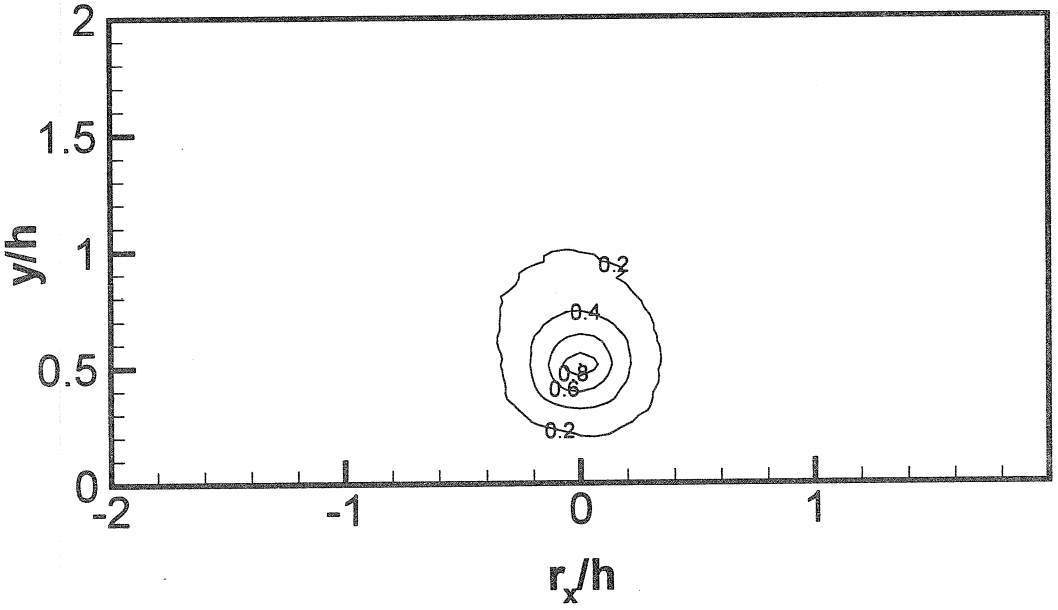

(b4)

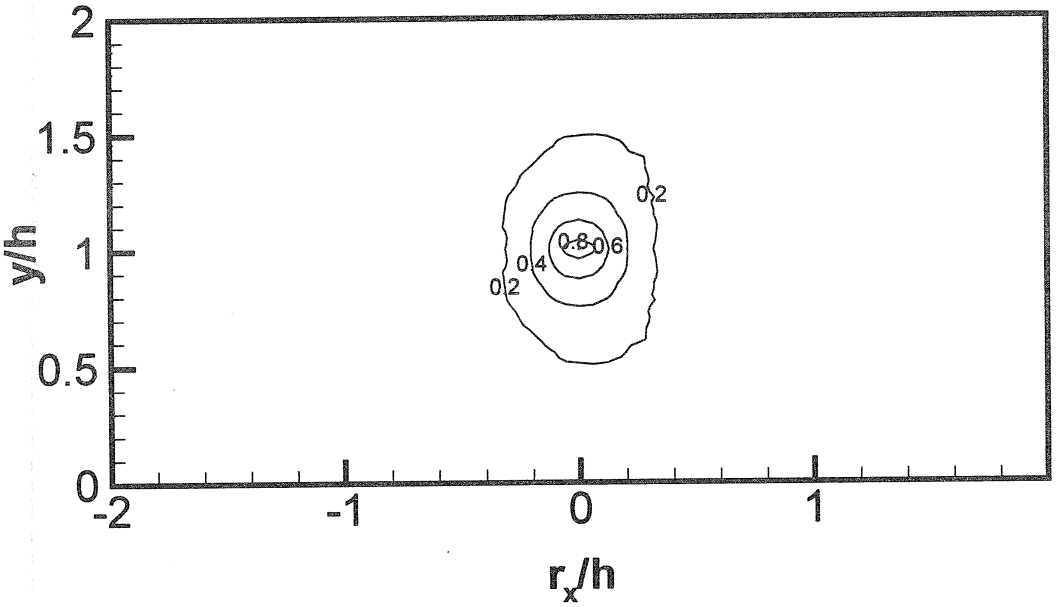

Figure 1. Contours of the two-point auto-correlation coefficients for Re_h = 5,378. (a1) - (a4), $R_{uu}(r_x,y,y')/\sigma_u(y)\sigma_u(y')$; (b1) - (b4), $R_{vv}(r_x,y,y')/\sigma_v(y)\sigma_v(y')$. The locations of the fixed correlating points are: (a1) - (b1), y/h = 0.065 (y^+ = 20.5); (a2) - (b2), y/h = 0.237 (y^+ = 75); (a3) - (b3), y/h = 0.508 (or y^+= 160); (a4) - (b4), y/h = 1.0 (or y^+ = 315).

(a1)

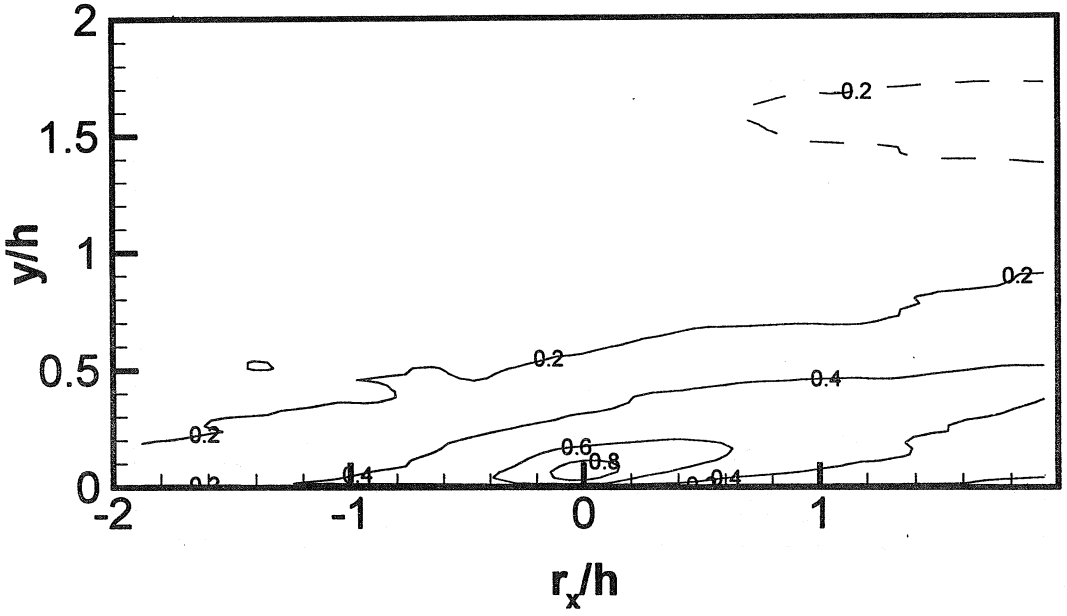
2
1.5
1
0.5
0
y/h
-2
-1
0
1
r_x/h
0.2
0.2
0.2
0.4
0.6
0.8
0.4

(a2)

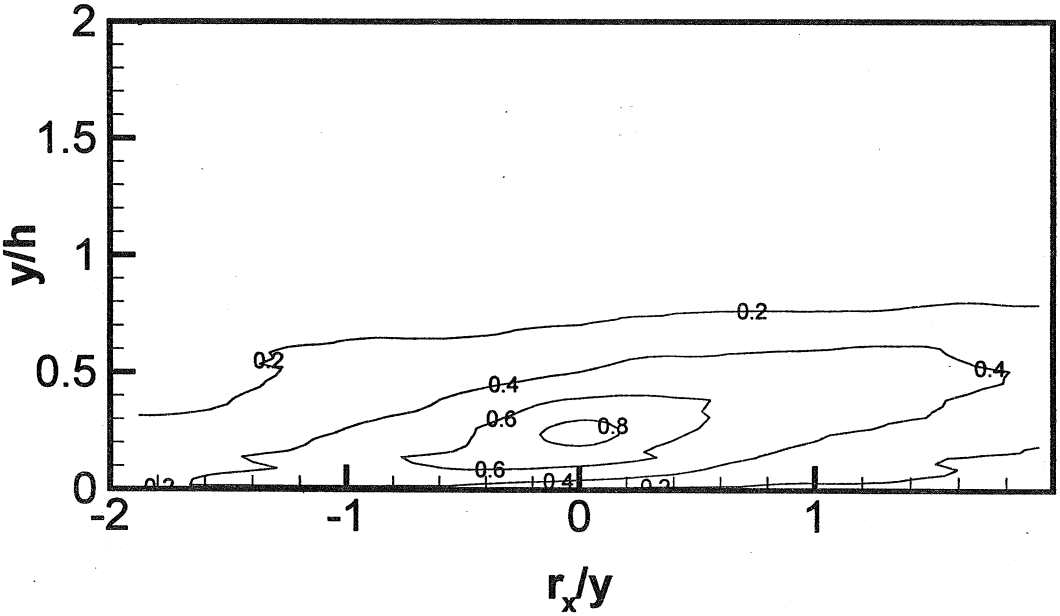
2
1.5
1
0.5
0
y/h
-2
-1
0
1
r_x/y
0.2
0.2
0.4
0.4
0.6
0.8
0.6

(a3)

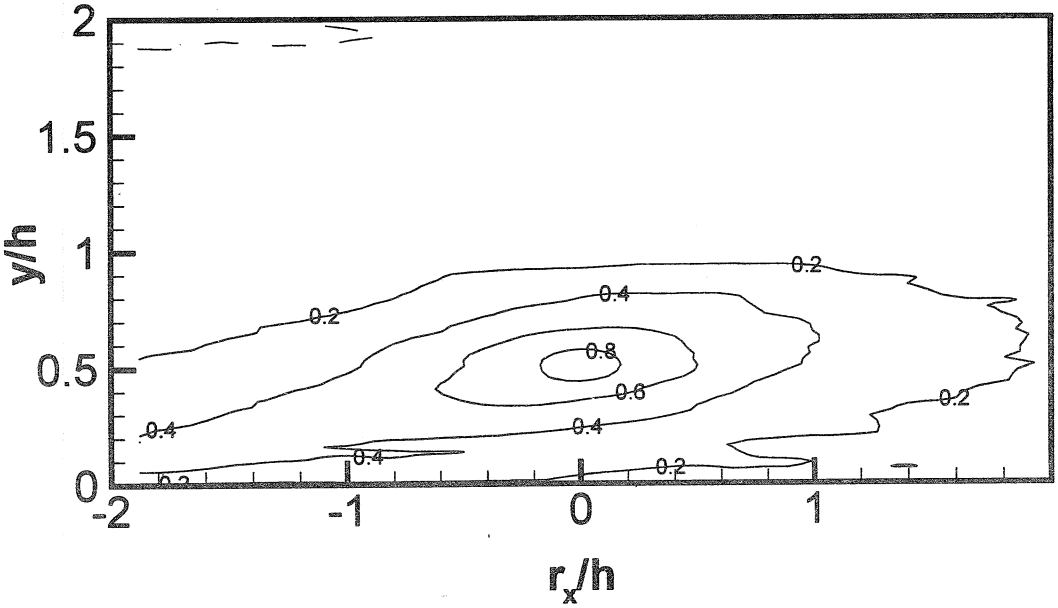

(a4)

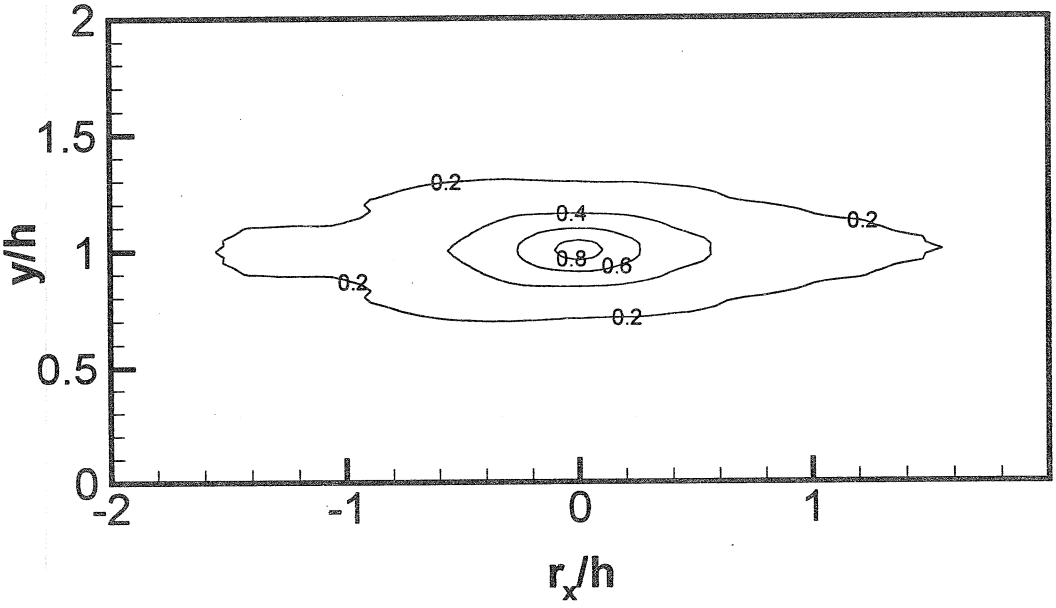

(b1)

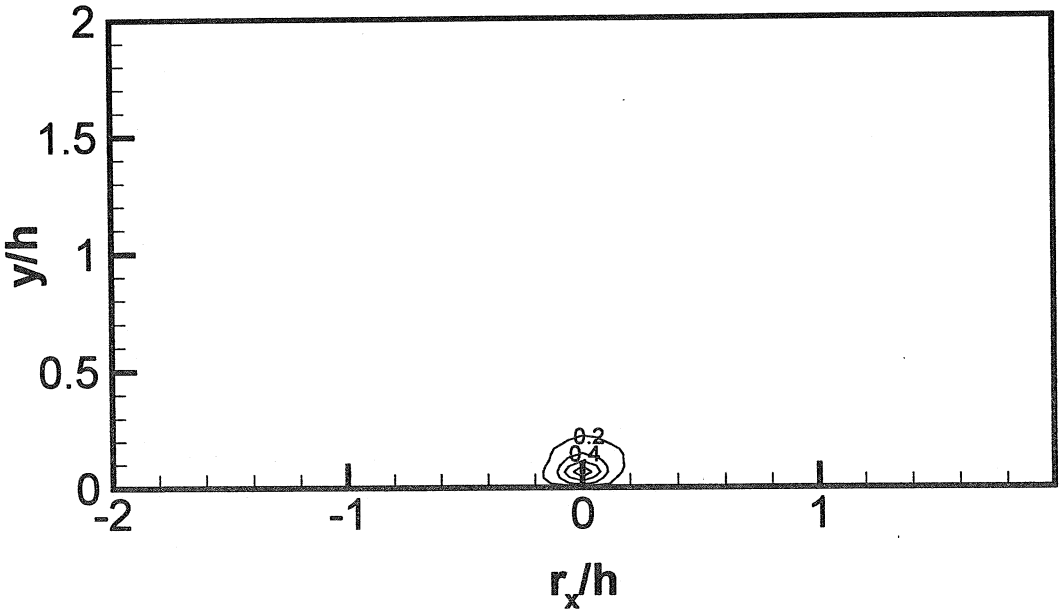

(b2)

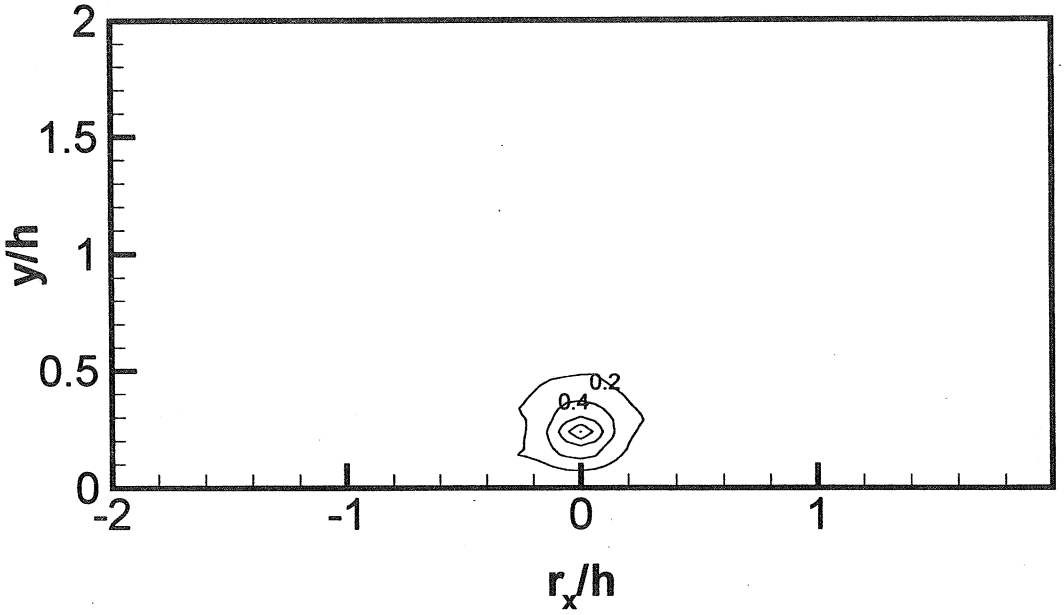

(b3)

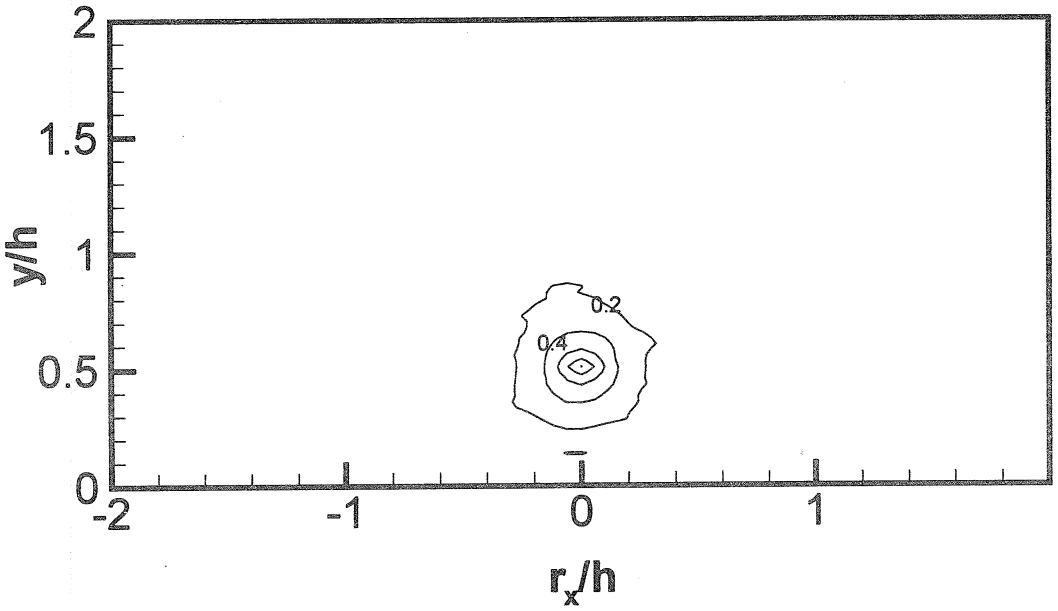

(b4)

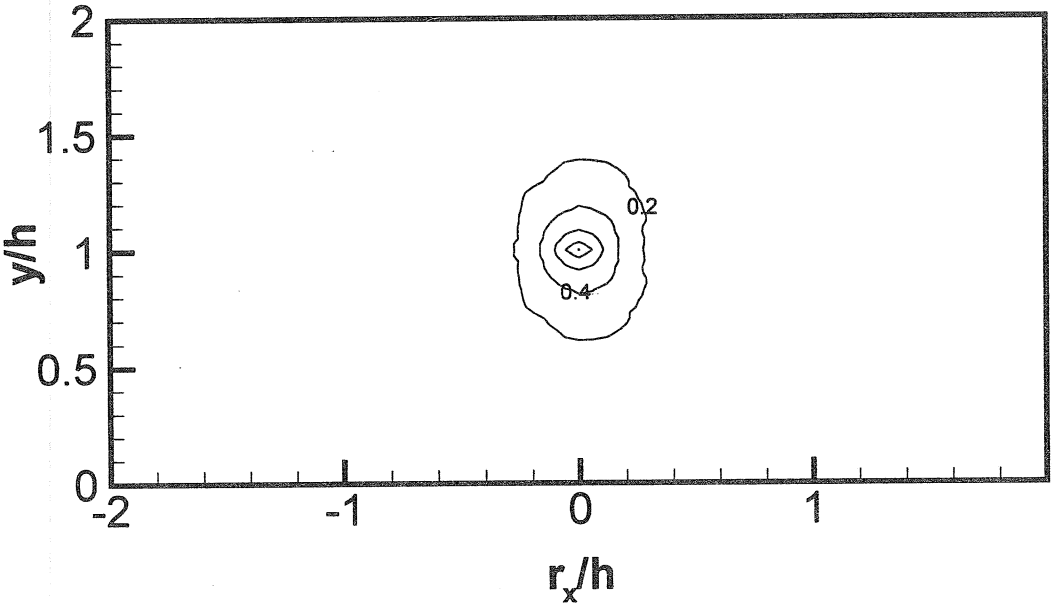

Figure 2. Contours of the two-point correlation coefficients for Re_h = 29,935. (a1) - (a4), $R_{uu}(r_x,y,y')/\sigma_u(y)\sigma_u(y')$; (b1) - (b4), $R_{vv}(r_x,y,y')/\sigma_v(y)\sigma_v(y')$. The locations of the fixed correlating points are the same as in Fig. 2.

excess of $4h$, c.f. Fig. 2(a3) and Fig 3(a2) and (a3). Auto-correlations of the v-component also grow as the fixed point moves away from the wall. This is consistent with Townsend's (1976) attached eddy hypothesis which states, in part, that eddies extend down to the wall, so that eddies centered at y have wall-normal scale of order y. But the v-correlations have roughly circular contours, in shape contrast to the elongated contours of the u-component auto-correlation.

The v-correlations are also short relative to the u-correlations. For example, for the fixed point at $y/h = 0.237$ the length of the region in which the u-correlation coefficient exceeds 40% is $1.5h$ (126 viscous wall units) in Fig. 1(a2) while the corresponding length of the v-correlation coefficient in Fig. 1(b2) is only $0.4h$, a ratio of almost 4:1. At the higher Reynolds number the length of the u-correlation is $3.4h$ compared to $0.3h$ (424 viscous wall units) for the v-correlation, a ratio of more than 10:1. Although the extent of the v-correlation, of order 0.3 - $0.4h$, is relatively small, the motions associated with the v-component are still large scale, in the sense that they scale with h. Inspection of the u-v cross-correlations reveals that they are elongated, much like the u-correlations (although somewhat shorter). This suggests that the largest scale motions contain a significant fraction of the Reynolds shear stress and only a small fraction of the v-component energy, but one must perform proper orthogonal decomposition to evaluate the exact amounts.

Cross-correlation coefficients have negative values around the fixed point, and with zero separation, the coefficients are approximately -0.41 over most of the channel. When the fixed point is on the centerline of the channel the cross-correlation coefficients are anti-symmetric with respect to y. When the fixed point is off of the centerline, the anti-symmetry persists to the extent that the correlation coefficients tend to have opposite sign above and below the centerline. Thus, second quadrant events in the lower half of the channel which produce strong negative values of the uv-product, tend to be associated with positive uv-events in the upper half of the channel. Note that the latter is equivalent to a second quadrant event since the normal to the upper wall is in the downward direction.

4.2 Eigenfunctions and eigenvalue spectra

Equation (7) was solved for the eigenfunctions and eigenvalues for each k using trapezoidal quadrature and an IMSL eigenproblem subroutine. The number of eigenmodes in the decomposition was 5,346, with 33 modes (k = 0 - 32) in the streamwise homogeneous direction and 162 modes (n = 1 - 162) in the wall-normal direction.

The eigenfunctions for the two Reynolds numbers with the domain of $2h$ are plotted in Figs. 3 for eigenmodes k = 0, 1 and n = 1, 2, 3, 4. Recalling that x denotes the streamwise coordinate normalized by L_x, and y denotes the wall-normal coordinate normalized by $2h$, the non-dimensional eigenfunctions of the two-dimensional decomposition are $(hL_x)^{1/2}\phi_i^{(k,n)}(y)$ and the non-dimensional eigenvalues are $\lambda^{(k,n)}/(u_\tau^2 hL_x)$. The factor of $(hL_x)^{1/2}$ is determined by the orthogonality of eigenfunctions (13) and the factor $(u_\tau^2 hL_x)$ comes from equation (7). The imaginary parts of all $k = 0$ eigenmodes are zero, but for $k > 0$ the eigenfunctions are complex. The figures show only the real parts. Both real and imaginary parts of eigenfunctions contribute to the energy and Reynolds stress associated with each eigenmode. The phases between eigenfunctions of the u- and v-components do not influence the contributions of the eigenmodes to the turbulent kinetic energy. However, they are very important in determining the contributions of the eigenmodes to the Reynolds stress, as can be seen from equation (15). The phases are mostly opposite in sign in the lower half of the channel and have the same sign in the upper half of the channel. This results in positive contributions to the Reynolds stress in both halves of the channel.

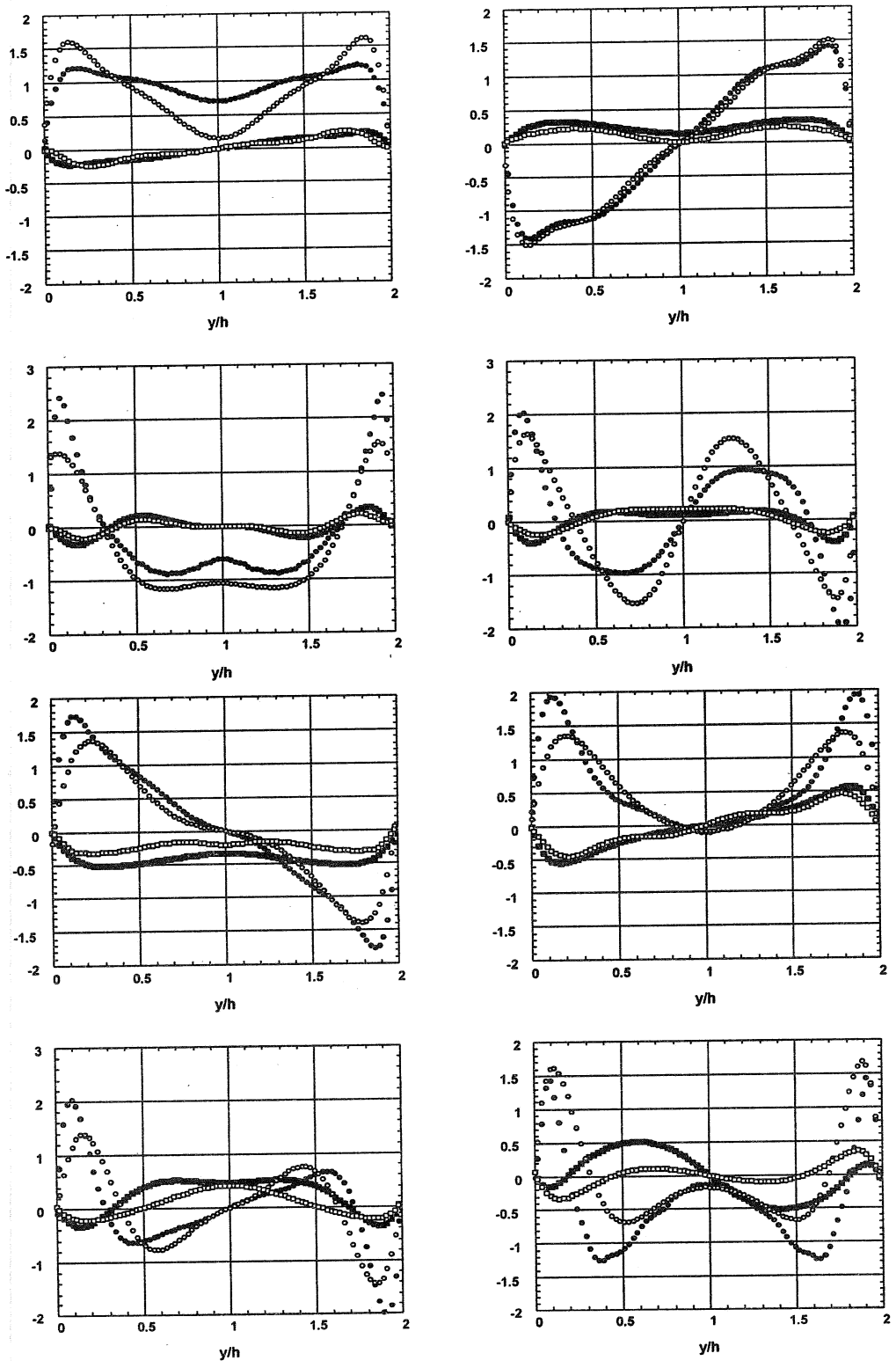

Figure 3. The real part of the two-dimensional eigenfunctions for various mode orders (k, n). ○, $(hL_x)^{1/2}\phi_u^{(k,n)}(y)$; □, $(hL_x)^{1/2}\phi_v^{(k,n)}(y)$. Solid symbols represent Re_h = 5,378, and open symbols represent Re_h = 29,935.

The eigenfunctions for both components are alternately symmetric and anti-symmetric about the center of the channel for successive orders of the wall-normal modes and streamwise modes. For each eigenmode, the symmetries of the eigenfunctions for the two components are always opposite. As a consequence, contributions of each of the eigenmodes to the Reynolds stress are mostly positive. There is a simple rule which can be used to identify the symmetry of the eigenfunctions in terms of eigenmode orders k and n. If $(k + n)$ is odd, the eigenfunctions for the u-component are symmetric and the eigenfunctions of the v-component are anti-symmetric. If $(k + n)$ is even, the opposite is true. This feature of the eigenfunctions reveals that contributions to the Reynolds stress are statistically positive, and that both the upper and the lower halves of the channel are statistically identical.

Equations (14) - (16) can be used to evaluate the contributions of the different eigenmodes and hence different scales of eddies, to the energy and the Reynolds stress. Each mode makes its contribution independently because of the orthogonality of the eigenfunctions. The $k = 0$ modes require careful interpretation. From equations (2) and (3) the $k = 0$ modes are given by

$$\hat{u}_i(0,y) = \int_0^1 u_i(x,y)dx = \frac{1}{L_x}\int_0^{L_x} u_i(xL_x,y)d(xL_x) = \sum_n a^{(0,n)}\phi_i^{(0,n)}(y) \quad . \tag{17}$$

Thus, the $(0, n)$ eigenfunctions represent decomposition of the line average of the fluctuating velocity over the streamwise length of the domain, L_x. If L_x were infinite, ergodicity of line averages in the homogeneous streamwise direction would imply that the line average of each fluctuating velocity component is zero, and hence all $(0, n)$ modes would vanish. When L_x is finite, the integral in (17) can be interpreted as a running average, which acts as a low pass filter. All modes of wavelength L_x or less integrate to zero, so the $k = 0$ modes represent the contribution from all motions whose wavelengths are longer than L_x.

Table 3 gives the fractional contribution of each eigenmode of order (k, n) to the total energy. They are energy-ordered for the $Re_h = 5{,}378$ modes. Table 4 gives the fractional contribution of each eigenmode to the total Reynolds stress as calculated from Equation (16) by integrating the eigenfunction products across the channel. The contributions are arranged in descending order for the $Re_h = 5{,}378$ modes (the descending ordering is slightly different for the high Reynolds number). Both of these quantities represent contributions to the total value integrated across the channel. The (0, 1) modes for $Re_h = 5{,}378$ and 29,935 contain 10.5% and 13.8% of total energy, respectively, and they are the strongest contributors to the energy. The largest contributors to the total Reynolds stress are the (0, 2) modes, which contain 13.3% and 13.6% of total Reynolds stress for $Re_h = 5{,}378$ and $Re_h = 29{,}935$. The first six modes ($k = 0$ - 2, $n = 1$ - 2) out of total 5,346 eigenmodes contribute more than one third of total energy and one half of total Reynolds stress for both Reynolds numbers. *The first 12 eigenmodes ($k = 0$ - 2, $n = 1$ - 4) contain almost one half of the total energy and two-thirds to three-quarters of the total Reynolds stress.* These modes consist of structures whose lengths in the streamwise direction are $L_x = 3.2h$ ($k = 1$) and $L_x/2 = 1.6h$, and all modes longer than L_x ($k = 0$), In the y-direction the length scales associated with the modes $n = 1$ - 4 range from $2h$ down to $0.3h$ (c.f. Fig.3), which are still large, considering that the thickness of the logarithmic layer is no more than $0.2h$.

These results compare well with direct numerical simulations of channel flow at low Reynolds numbers. Sirovich, *et al.*, (1990) give the eigenvalue spectrum for three-dimensional decomposition of very low (barely transitional) Reynolds number ($Re_h = 1{,}500$, $h^+ = 80$). Summing over the first four modes in the spanwise direction gives an approximate two-dimensional decomposition that can be compared to the present results. The first six most energetic modes are identical to those found in Table 3, but they contain rather more energy,

Table 3: Fractional contributions of the 2-D eigenmodes to the total turbulent kinetic energy for Re_h = 5,378 and 29,935. The eigenmode indices are denoted by (k, n). The table was arranged in a descending order of the energy contributions at low Reynolds number, Re_h = 5,378. D is the degeneracy of eigenmode in the streamwise direction.

		Fractional energy, %		
Order	**(k, n)**	**Re_h = 5,378**	**Re_h = 29,935**	**D**
1	(0, 1)	10.5	13.8	1
2	(0, 2)	8.92	9.08	1
3	(1, 1)	5.28	5.81	2
4	(1, 2)	4.92	4.87	2
5	(1, 3)	3.54	3.28	2
6	(0, 3)	2.86	2.58	1
7	(0, 4)	2.64	1.93	1
8	(2, 1)	2.39	2.03	2
9	(1, 4)	2.36	2.24	2
10	(2, 2)	1.72	1.84	2
11	(1, 5)	1.61	1.15	2
12	(0, 5)	1.41	1.25	1
13	(2, 3)	1.29	1.3	2
14	(1, 6)	1.21	1.12	2
15	(2, 4)	1.17	0.94	2
16	(0, 6)	1.15	0.50	1
17	(3, 1)	1.1	1.0	2
18	(1, 7)	0.95	0.60	2
19	(3, 2)	0.91	1.0	2
20	(3, 3)	0.91	0.69	2
6 modes	(0 - 2, 1 - 2)	33	37	
12 modes	(0 - 2, 1 - 4)	48	50	

67% versus 33% at Re_h = 5,378. At approximately twice the Reynolds number (Re_h = 2,800, h^+ = 180) one-dimensional POD on the half-channel domain ($0 < y^+ < 180$) gives 32% of the total kinetic energy and 66% of the Reynolds stress in just the first three modes (Moin & Moser 1989). The dominance of the lower order modes in the direct numerical simulations was not surprising, because the spectrum of the turbulence has a fairly small range of scales at low Reynolds numbers. However, the relatively similar behavior of the present results at substantially higher Reynolds numbers indicates that dominance of the large-scale modes persists, even as the spectrum widens.

The fact that the largest-scale motions in streamwise and wall-normal directions are the most important contributors to the turbulent kinetic energy is consistent with the early

observations of Grant (1958) and Townsend (1958) and subsequent investigations, which were also at moderate Reynolds numbers. The fact that these scales also carry more than two-thirds of the total Reynolds shear stress is quite surprising, and completely at odds with the notion that the large scales are not important to the transport of momentum and hence "inactive" (Townsend 1976). Even the first 6 modes that contain 33 - 37% of the kinetic energy contain 50 - 56% of the Reynolds shear stress. The inescapable conclusion is that large-scale motions play a very important role in the transport of momentum, at least for the range of Reynolds numbers considered here.

Table 4: Fractional contributions of the 2-D eigenmodes with a domain of $2h$ to the total Reynolds stress for Re_h = 5,378 and 29,935. The eigenmode indices are denoted by (k, n). The table was arranged in a descending order of the Reynolds stress contributions at low Reynolds number, Re_h = 5,378. D is the degeneracy of eigenmode in the streamwise direction only.

		Fractional Reynolds stress, %		
Order	**(k, n)**	**Re_h = 5,378**	**Re_h = 29,935**	**D**
1	(0, 2)	13.3	13.6	1
2	(1, 1)	12.28	9.2	2
3	(0, 1)	10.81	7.81	1
4	(1, 2)	9.16	10.2	2
5	(2, 1)	6.25	5.56	2
6	(1, 3)	4.92	0.24	2
7	(2, 2)	4.3	3.95	2
8	(1, 4)	3.8	3.77	2
9	(2, 4)	3.03	1.72	2
10	(0, 4)	2.88	2.4	1
11	(3, 1)	2.69	2.76	2
12	(0, 3)	2.5	1.26	1
13	(3, 3)	2.29	1.36	2
14	(3, 2)	2.22	3.95	2
15	(2, 3)	2.02	2.11	2
16	(4, 1)	1.73	1.57	1
17	(1, 6)	1.71	1.28	2
18	(4, 2)	1.3	1.28	2
19	(3, 4)	1.28	0.186	2
20	(1, 5)	0.734	0.254	2
6 modes	(0 - 2, 1 - 2)	56	50	
12 modes	(0 - 2, 1 - 4)	75	67	

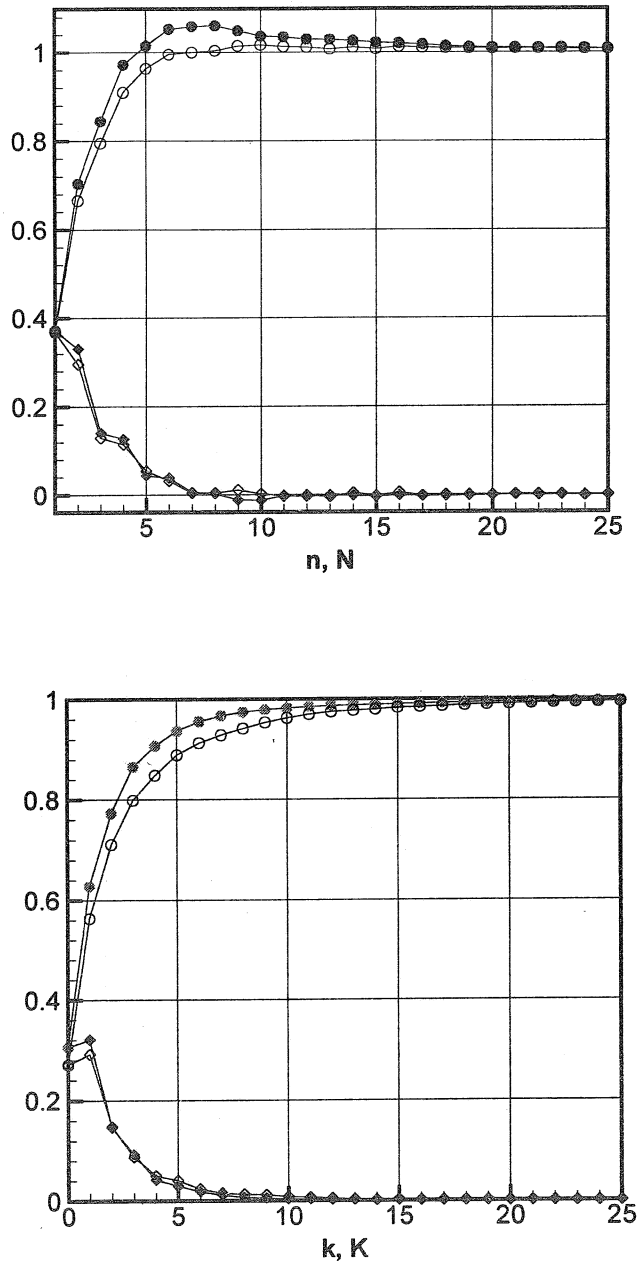

Figure 4. Fractional Reynolds stress contributions. (a) circles, $\Sigma_{\text{all } k}\langle uv\rangle^{(k,n)}$; diamonds , cumulative Reynolds stress of the first N wall-normal eigenmodes, $\Sigma_{\text{all } k}\Sigma_{n=1\text{-}N}\langle uv\rangle^{(k,n)}$; (b) circles, $\Sigma_{\text{all } n}\langle uv\rangle^{(k,n)}$; diamonds, cumulative Reynolds stress of the first K streamwise eigenmodes, $\Sigma_{\text{all } n}\Sigma_{k=0\text{-}K}\langle uv\rangle^{(k,n)}$. Solid symbols represent Re_h = 5,378, and open symbols represent Re_h = 29,935.

But, what about the small-scale motions, especially those in the near-wall buffer layer where they are most active? The contribution of higher order modes to the total Reynolds shear stresses is shown graphically in Fig. 4. For the lower modes shown in Table 4 the modes all contribute positively, but in general the contribution of a single mode to the Reynolds stress can

be positive or negative. Figure 4(a) gives the spectrum of total contributions to the Reynolds stress of modes, n, summed over all wavenumber, k, and the cumulative contributions of all modes with $n \leq N$. The lower order modes for Re_h = 5,378 actually overshoot the total mean value up to n = 8, after which slightly negative values return the total to 100% of the total contribution. A similar phenomenon was reported by Moin & Moser (1989). The overshoot does not occur at the higher Reynolds number. For both cases 10 modes suffice to carry all of the Reynolds shear stress. Figure 4(b) gives the total contribution to the Reynolds stress for different Fourier modes, k, summed over all Karhunen-Loeve modes, n, and the cumulative contributions for $k \leq K$. The first four n modes (n = 1 - 4) contribute 91 - 97%; the first four k modes (k = 0 - 3) contribute 80 - 87% of the Reynolds stress.

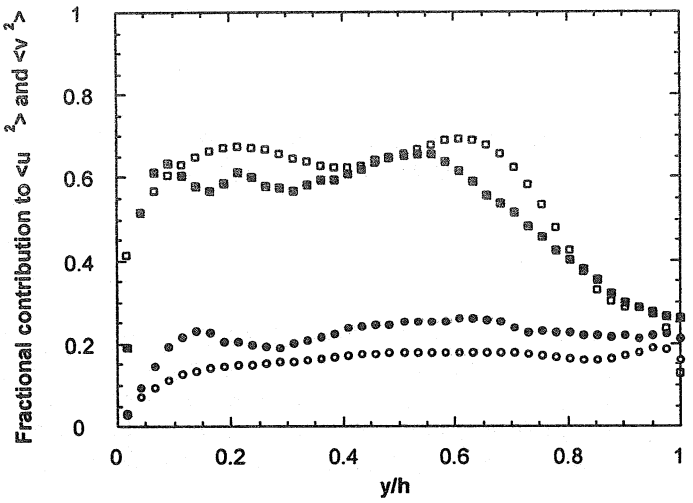

Figure 5. Profiles of the fractional contributions of the first 12 eigenmodes (k = 0 - 2, n = 1 - 4) to the kinetic energies of streamwise, □, and wall-normal, ○, velocities. Solid symbols represent Re_h = 5,378, and open symbols represent Re_h = 29,935.

As indicated earlier the contributions inferred from the eigenvalues refer to the total values of the kinetic energy and the Reynolds stress integrated across the channel. It is possible for the large-scale motions to dominate the integrated value while the small-scale dominate locally in a region such as the buffer layer. Figure 5 presents the *local* fractional contributions to the total energy of the streamwise and wall-normal components by the 12 eigenmodes with k = 0 - 2 and n = 1 - 4. Figure 6 gives the corresponding local fractional contributions to the Reynolds stress. The contributions of these 12 modes to the *total* energy are about 50%, but this is divided between a large contribution to streamwise kinetic energy of about 60% for y/h = 0.05 – 0.6, and a much smaller contributions to the wall-normal kinetic energy of about 20% for y/h > (0.1 - 0.2). Thus, most of the streamwise kinetic energy below y/h = 0.6 is large-scale, but the strong majority of the wall-normal kinetic energy is small-scale. In the channel center contributions of both components are approximately equal. These results are consistent with the observation that a smaller numbers of the large-scale structures reach the centerline. In contrast Figure 6 shows that $\langle uv \rangle$ receives strong contributions from large scales at the centerline. This suggests that the Reynolds stress events are intermittent in the region of the centerline.

The local contributions of the 12 eigenmodes with k = 0 - 2 and n = 1 – 4 to the local Reynolds stress are 60 to 80%, except for the region close to the wall, Fig. 6. This implies that the low mode (large-scale) motions are quite energetic and not 'inactive' in generating turbulence

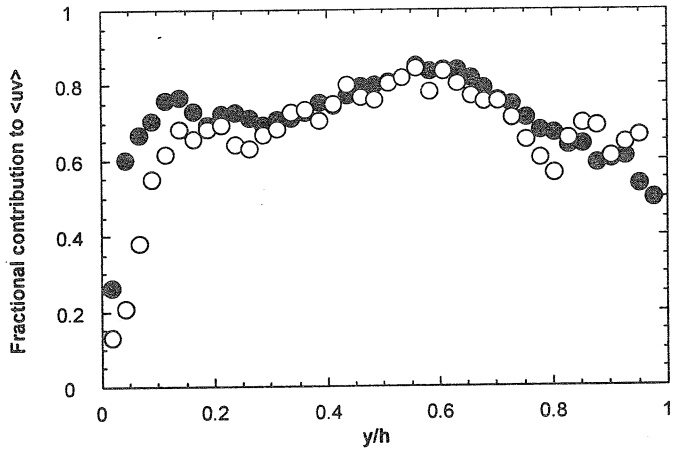

Figure 6. Profiles of the fractional contributions of the first 12 eigenmodes ($k = 0$ - 2, $n = 1 - 4$) to the Reynolds shear stress. Solid symbols represent Re_h = 5,378, and open symbols represent Re_h = 29,935.

above the buffer layer. In the near-wall region the contributions of the large-scales are much smaller. Because of the limited spatial resolution of the measurements relative to the scales in this region, the values shown in Figs. 5 and 6 are only estimates of the precise contributions. Evenso, the fractional contribution to the near-wall Reynolds shear stress lies in a range of 13-26% that is consistent with an estimate of 15% by Naguib and Wark (1999).

4.3 Velocity fields of the large-scale flows

We turn now to the question of determining the flow patterns associated with the large-scale energetic modes. To be specific, we shall seek the structure of the flows that create the contributions from the first twelve modes, containing about one-half of the kinetic energy, and two-thirds of the Reynolds shear stress. The individual eigenfunctions cannot, by themselves, describe the structure of an eddy, because eddies are composed of many modes. This is especially clear for homogeneous turbulence in which the eigenfunctions are simple trigonometric waves. Lumley's (1970) characteristic eddy method attempts to define a single characteristic eddy by projecting the modal structure on a shot noise model of randomly scattered eddies, but this approach suffers from a fundamental ambiguity in which the phases of the complex eigenfunctions are left undetermined (Min & Moser 1989). This problem does not arise if one simply phrases the question as one of determining the structure of the eddies that contribute to certain modes, for then the phases of each mode are found directly by projecting the instantaneous velocity fields onto the group. For the present work, this approach is particularly appropriate, because we have already the modes that are of interest. Of course, other groups of modes could also be identified, but they would be associated with different questions.

4.3.1 Vector structure of the modes

Although individual modes cannot fully describe an eddy, their structure is of interest, nonetheless, as the components of the complete structure. From equations (3) and (6) the component of the fluctuating velocity component associated with the (k, n) mode is

$$u_i^{(k,n)}(x,y) = \mathrm{Re}\, a^{(k,n)}\, \mathrm{Re}\, \psi_i^{(k,n)}(x,y) - \mathrm{Im}\, a^{(k,n)}\, \mathrm{Im}\, \psi_i^{(k,n)}(x,y). \qquad (19a)$$

It is easy to show that the vectors for the imaginary eigenfunctions are the real eigenfunction vectors $\psi_i^{(k,n)} = (\psi_1^{(k,n)}, \psi_2^{(k,n)}$ with a $\pi/2$ phase shift, corresponding to a dimensional spatial shift of $L_X/4k$. Then the (k, n) mode component of the velocity is

$$u_i^{(k,n)}(x,y) = \mathrm{Re}\, a^{(k,n)}\, \mathrm{Re}\, \psi_i^{(k,n)}(x,y) - \mathrm{Im}\, a^{(k,n)}\, \mathrm{Re}\, \psi_i^{(k,n)}(x - 1/4k, y) \qquad (19b)$$

The eigenfunctions can be presented in a vector form, since the two components ψ_1 and ψ_2, are related to velocity components u_1 and u_2. A real eigenfunction vector can be defined as

$$\mathrm{Re}\, \psi^{(k,n)}(x,y) = (\mathrm{Re}\, \psi_1^{(k,n)}(x,y), \mathrm{Re}\, \psi_2^{(k,n)}(x,y)), \qquad (20a)$$

$$= (\mathrm{Re}[\phi_1^{(k,n)}(x,y) e^{j2\pi kx}]\, \mathrm{Re}[\phi_2^{(k,n)}(x,y) e^{j2\pi kx}]). \qquad (20b)$$

From (19b) the modal velocity can be constructed from a linear combination of the vector field of the real eigenfunction and the vector field of the real eigenfunction shifted by $1/4k$. Thus, it suffices to consider the vector fields given by equation (20).

Figure 7 presents the real eigenfunction vector fields for eigenmodes $k = 0$, 1 with $n = 1$, 2, and 3 for $Re_h = 5{,}378$. Every other vector has been removed to show the patterns more clearly. Because of homogeneity in the streamwise direction the structure of each eigenfunction is sinusoidal with phase $\theta(x) = 2\pi kx$. The structure in the inhomogeneous wall-normal direction is determined by the wall-normal eigenfunctions, $\phi_i^{(k,n)}(y)$, *c.f.* Eq. (20) and Fig. 3. Recall that the eigenfunction vectors of the $k = 0$ modes represent the projection of all modes having wavelengths longer than the fundamental wavelength of the domain, $3.2h$. They are independent of x, but the projected wall-normal component does not vanish, so the $k = 0$ modes still contribute to the Reynolds shear stress. The (0, 1) and (0, 3) modes are symmetric with respect to the centerline, while the (0, 2) mode is anti-symmetric.

The eigenfunction vector fields of the $k = 1$ modes in Fig. 7 are once-periodic in $3.2h$. They show motions like ejections (second-quadrant Q2 events) and sweeps (fourth-quadrant Q4 events) that are strong in a region inclined at about 35° to the wall. These motions contribute positively to the net mean Reynolds shear stress, the amount depending on the phase relationship between the u- and v- eigenfunctions. In Figs. 7(d) and (f) one can discern a recurring pattern consisting of an inclined Q2 event (along the locus of the straight line) in the lower half of the channel lying under a clockwise rotating motion (highlighted by the ellipse), and an inclined Q4 event lying under a counter-clockwise rotating spanwise vortex (highlighted by the second ellipse). The Q2 and Q4 flows create a stagnation point and an associated inclined shear-layer. The combination of a rotation about the spanwise direction, an inclined region of Q2 vectors with a local maximum Q2 event and the shear layer created by a weaker upstream Q4 event has been identified by Adrian, Meinhart and Tomkins (1999) as the signature of a flow pattern that carries large amounts of Reynolds shear stress and occurs frequently in turbulent boundary layers. They argued that these signatures are associated with flow in the central x-y plane of hairpin-like vortices inclined in the streamwise direction. The hairpin paradigm was used in a loose, generic sense to include hairpin, horseshoe and cane-like structures having the general shape of quasi-streamwise leg of concentrated vorticity inclined to the wall and turning over in the spanwise direction near its top (to account for the spanwise vortex observed in the x-y plane). The Q2 events with local maxima were associated with vortex induction of the head and legs of the hairpin.

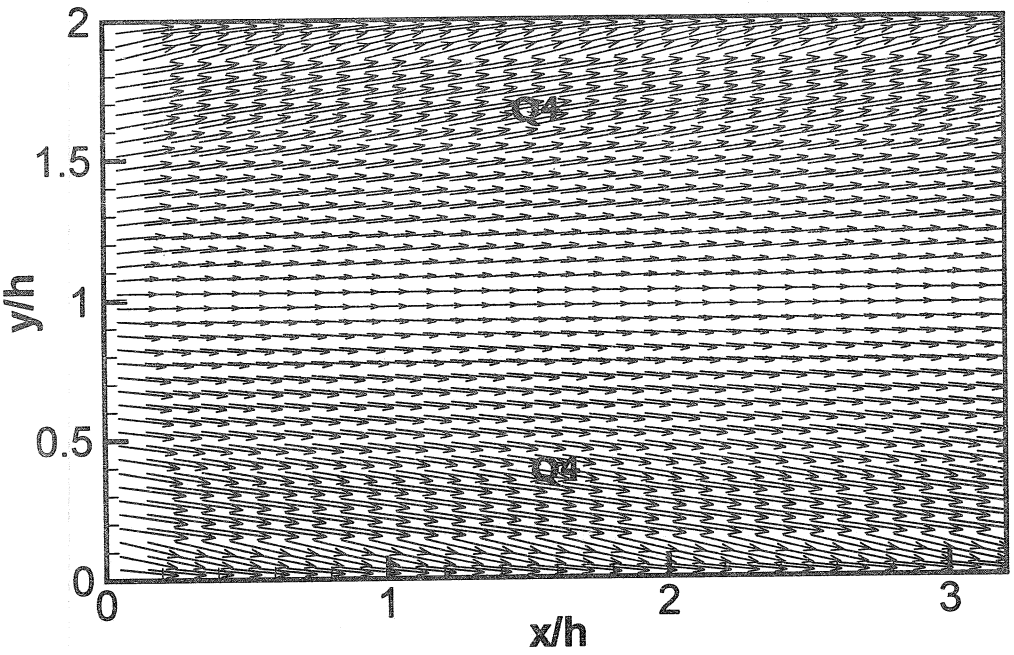

(a)

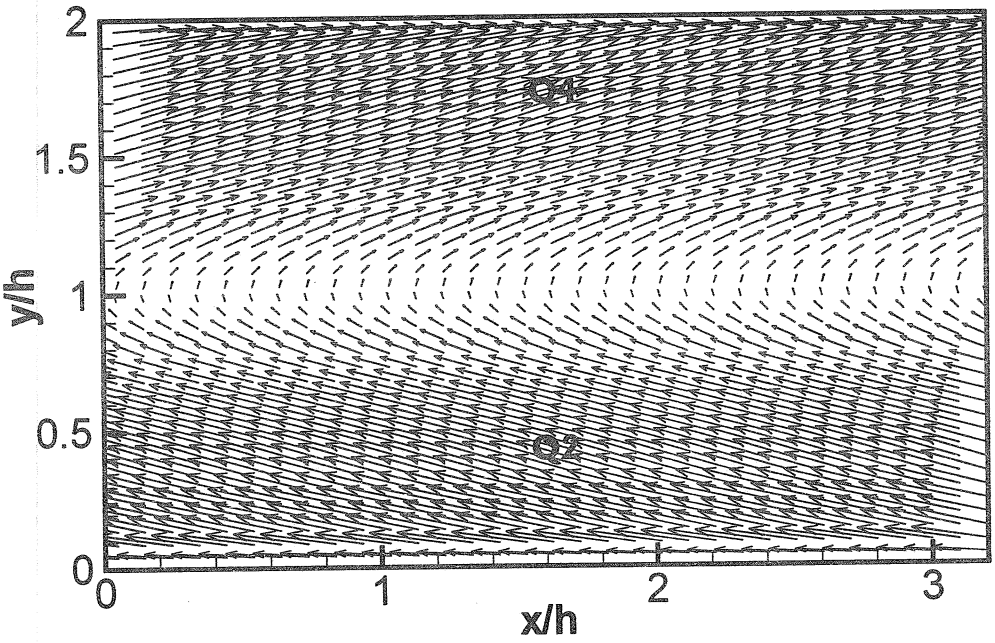

(b)

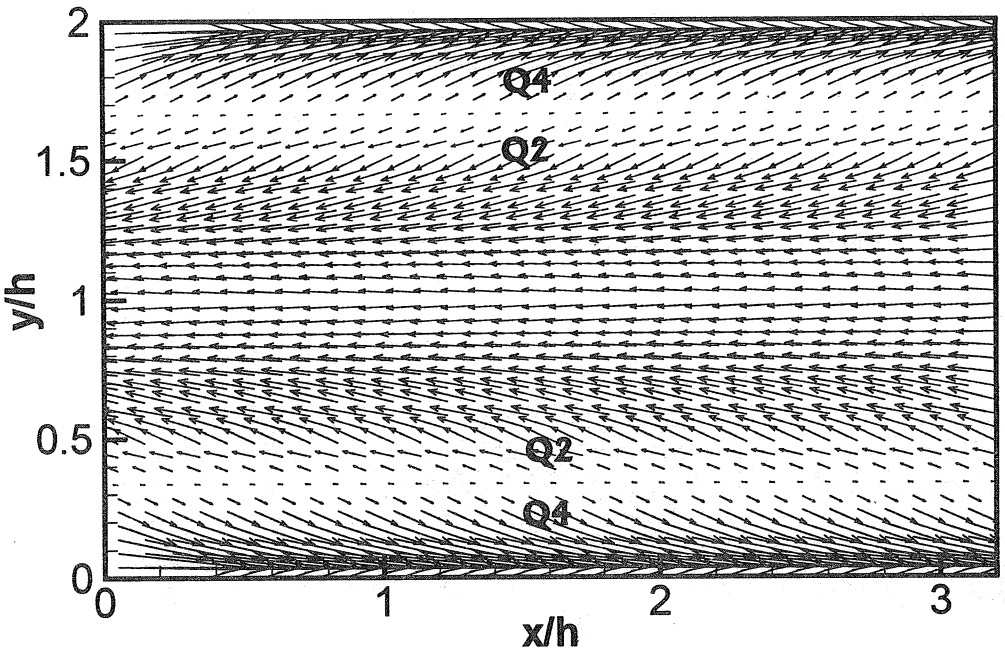

(c)

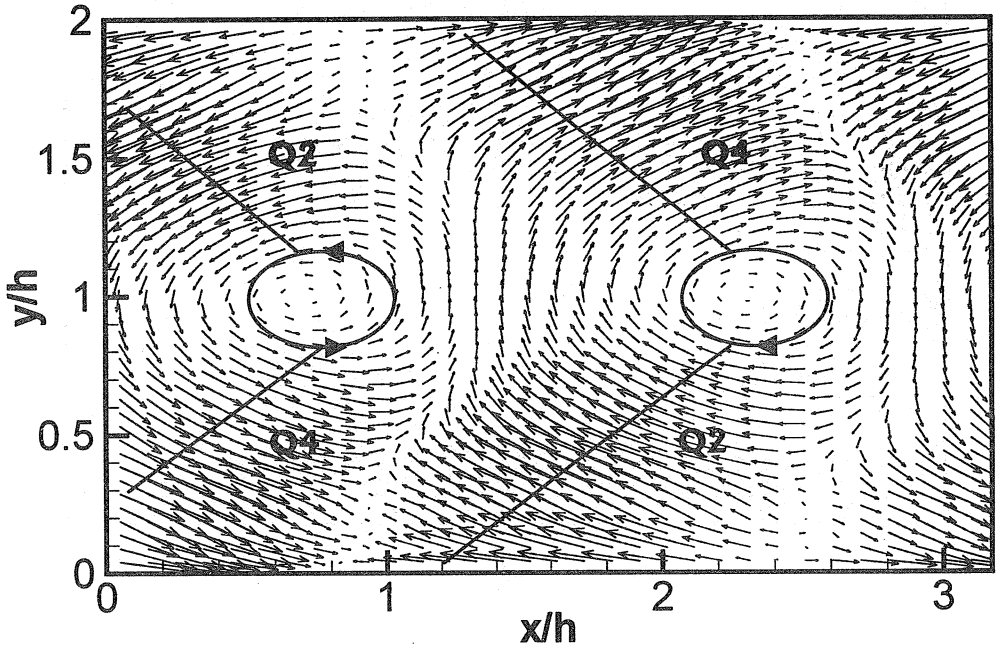

(d)

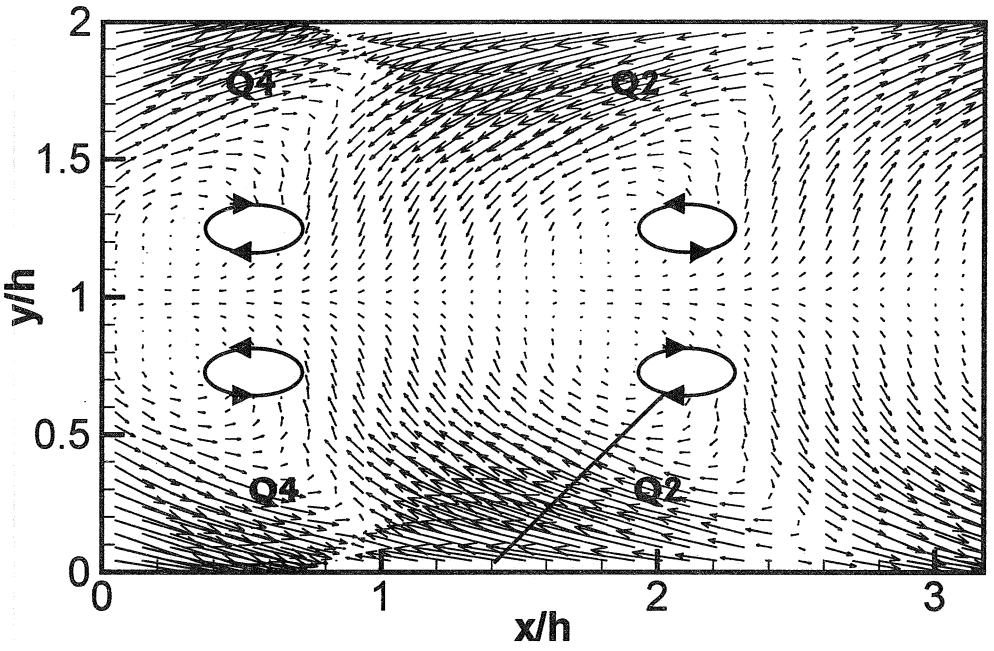

(e)

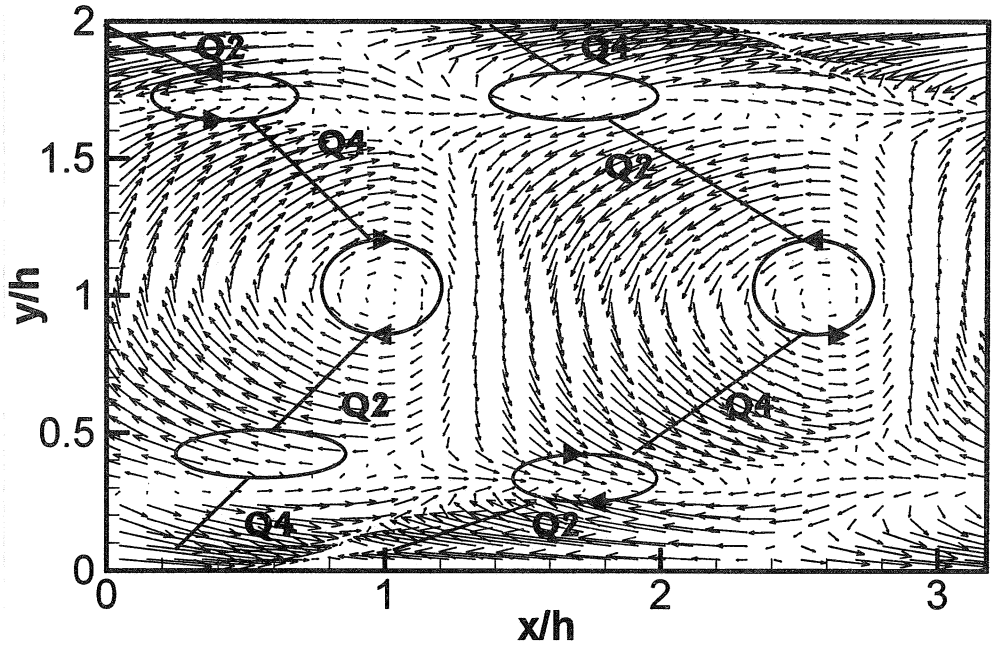

(f)

Figure 7. The eigenfunction vector fields of the first six most energetic modes for Re_h = 5,378. Mode order: (a) (k, n) = (0, 1); (b) (k, n) = (0, 2); (c) (k, n) = (0, 3); (d) (k, n) = (1, 1); (e) (k, n) = (1, 2); and (f) (k, n) = (1, 3).

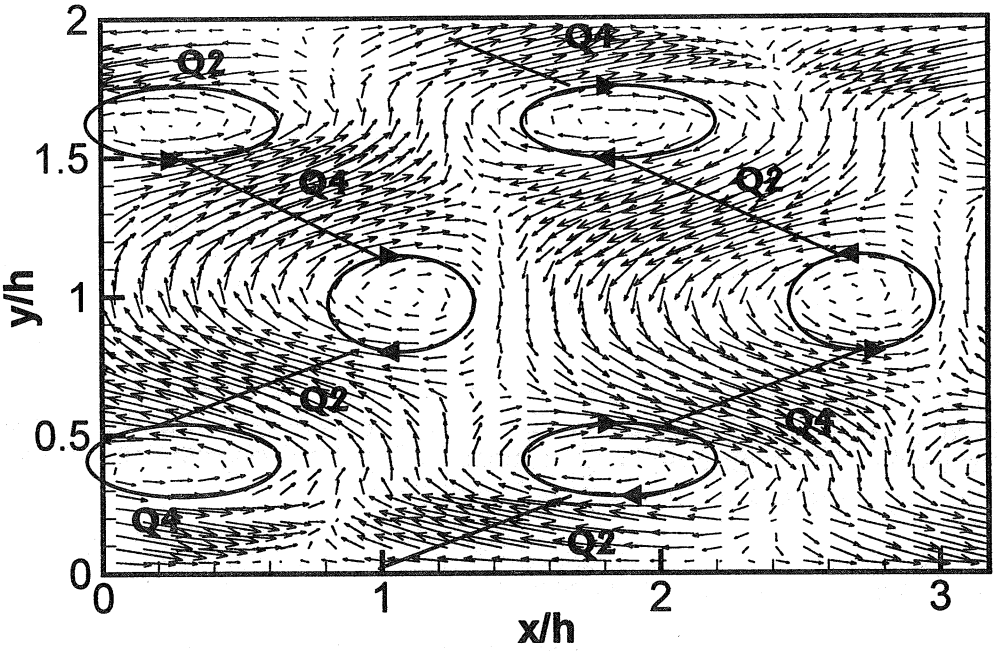

(a)

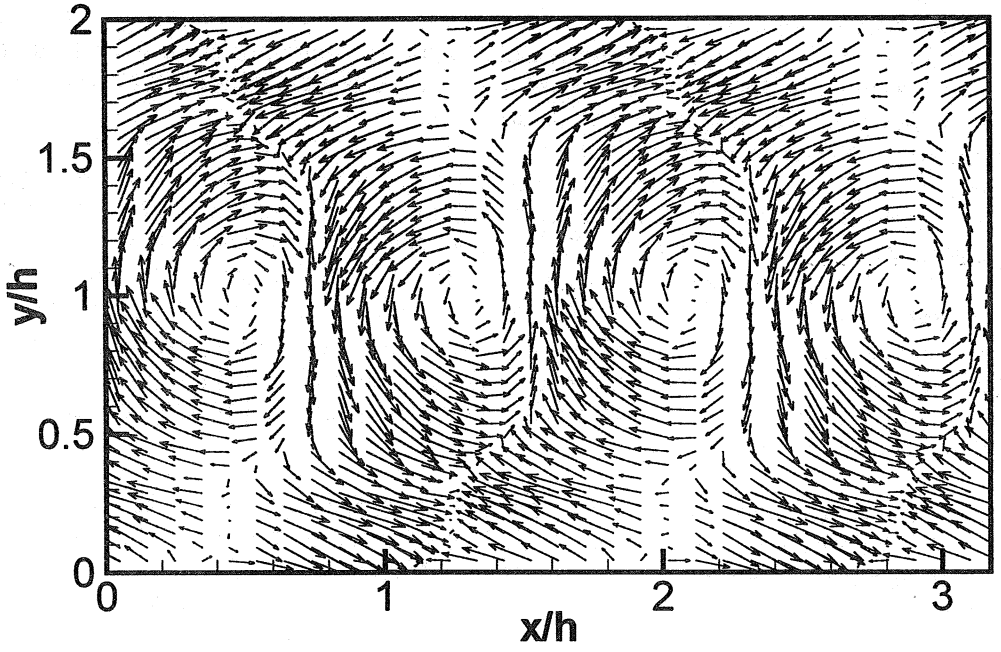

(b)

Figure 8. The eigenfunction vector fields for Re_h = 29,935 with mode order: (a) (k, n) = (1, 3); (b) (k, n) = (2, 2).

Since the purpose of the present paper is not to discuss the relevance of the hairpin paradigm, we shall refer to the flow pattern described above as the "signature of a characteristic Reynolds stress event".

Note that the reflectional symmetry with respect to the centerline in Fig. 7(e) results in regions of inclined Q2 and Q4 events that do not lie under a transverse vortex. Instead, the pattern looks like an in-plane convergence toward a three-dimensional saddle point with out-of-plane flow.

The eigenvector fields of the $Re_h = 29{,}935$ flow are very similar to those in Fig. 7 for $Re_h = 5.378$. One pattern, a (3,1) mode presented in Fig. 8(a), demonstrates the similarity that is typical of the other modes. The higher order (2,2) mode in Fig. 8(b) illustrates the increased layering that occurs in the y-direction as the modal order increases.

4.3.2. Velocity fields of the energetic, large-scale motion

To sample the types of eddies structures that are characterized by the low order eigenmodes, we have projected various snapshots of instantaneous fluctuating flow fields onto the 12 eigenmodes ($k = 0$ - 2, $n = 1$- 4). Representative samples of the random velocity fields taken from the data sets for each Reynolds number are shown in Fig. 9(a) and 10(a). The corresponding projected flow fields are displayed in Fig. 9(b) and 10(b). This procedure would fail to yield a clear picture of the eddies characterized by these modes if no such eddies were present in the sample realizations. However, Table 5 shows that the magnitudes of the Fourier coefficients $|a^{(k,n)}|$ for each projection are comparable to the root-mean-square values, as given by the square root of the eigenvalues. Therefore, eddies that are typical of the first twelve modes were present in each sample. (The phases of the Fourier coefficients for each random realizations are different, reflecting the dynamical behavior of the eigenmodes.) The projected fields in Fig. 9(b) and 10(b) each clearly contain two structures that possess all of the elements of the signature of a characteristic Reynolds stress event, as described above. A Q2 ejection of fluid from the wall with length scale of at least 500 viscous wall units ($1.6h$) in the streamwise direction and a strong Q4 motion of fluid from the outer region of the channel can be seen in the lower half of Fig. 9(b) for the lower Reynolds number. The Q2 and Q4 motions meet each other and generate a stagnation point/shear layer that extends from $y^+ = 100$ to 200 with an inclination angle of about 30° to 40° to the wall, in a manner very similar to that discussed above for the eigenmodes. A similar pattern coming down from the top wall appears to provide the Q4 motion for the downstream eddy on the lower wall.

The scales of the patterns in Fig. 9(b) are of the order of the channel height, but this is not very large in terms of the viscous length scale at the lower Reynolds number. The projection of the higher Reynolds number velocity field in Fig. 10(b) offers much more convincing evidence that these structures do scale with the outer length scale. Two signatures of large-scale characteristic stress event can be seen, one attached to the bottom wall and one attached to the top wall. To demonstrate further the similarity between large eddies at high and low Reynolds numbers, a second $Re_h = 29{,}925$ field is projected onto the lowest twelve modes in Fig. 10(c). This random snapshot is remarkably similar to the field in Fig. 9(b). The streamwise scales of the large motions exceed 2,000 viscous wall units, about $2h$, and their vertical size is about one channel half-height or $h^+ = 1{,}414$. Projection onto the first six modes instead of the first twelve modes has no qualitative effect and relatively little quantitative effect on the vector fields. Examination of the full data sets reveals that projections containing patterns that meet all of the criteria for the signature of a characteristic stress event occur over one-half of the time. Given

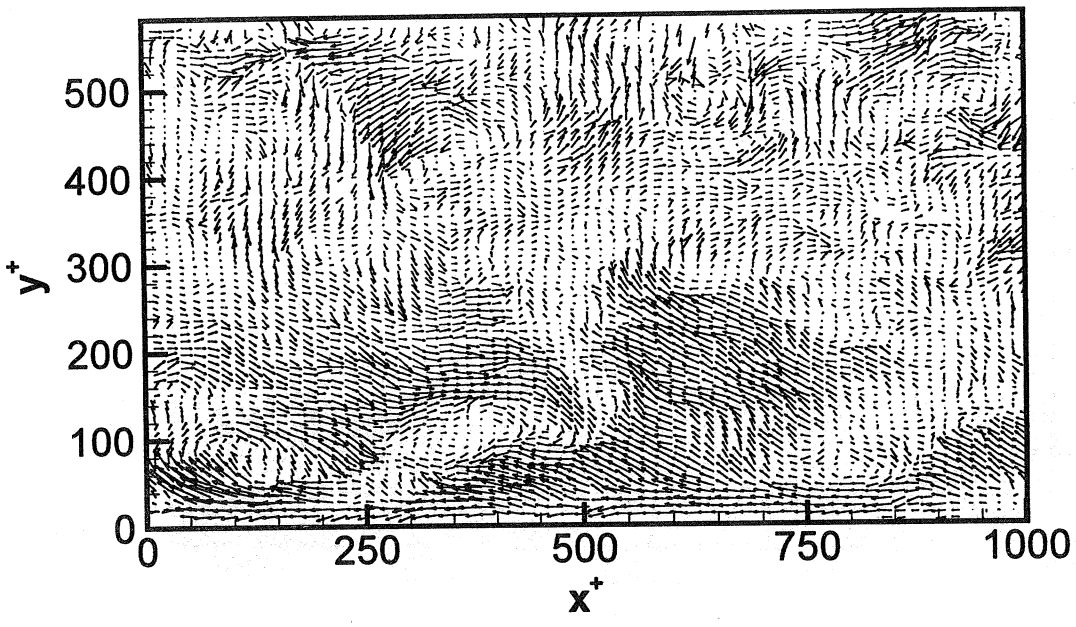

(a)

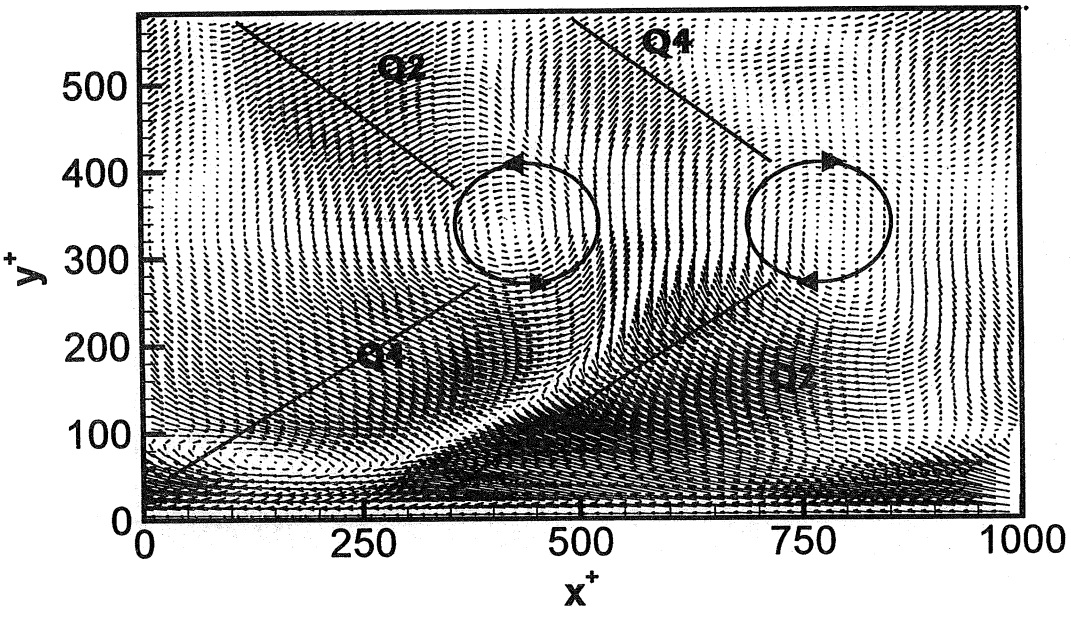

(b)

Figure 9. (a) An instantaneous turbulent fluctuating velocity field from PIV measurements at Re_h = 5,378; (b) The projection onto the first 12 eigenmodes (k = 0 - 2, n = 1 - 4).

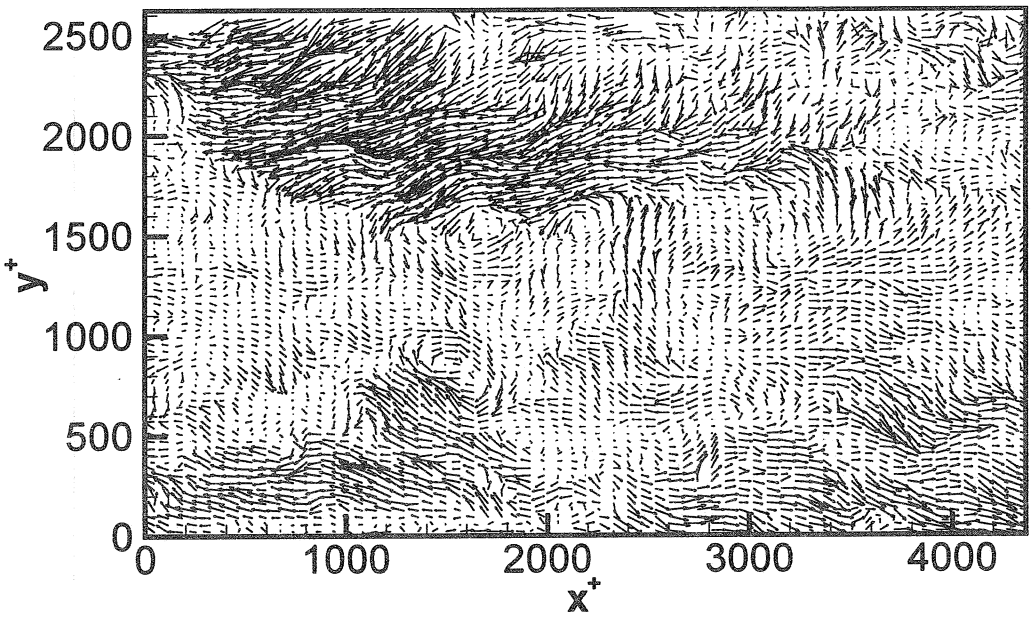
2500
2000
1500
1000
500
0
y+
0
1000
2000
3000
4000
x+

(a)

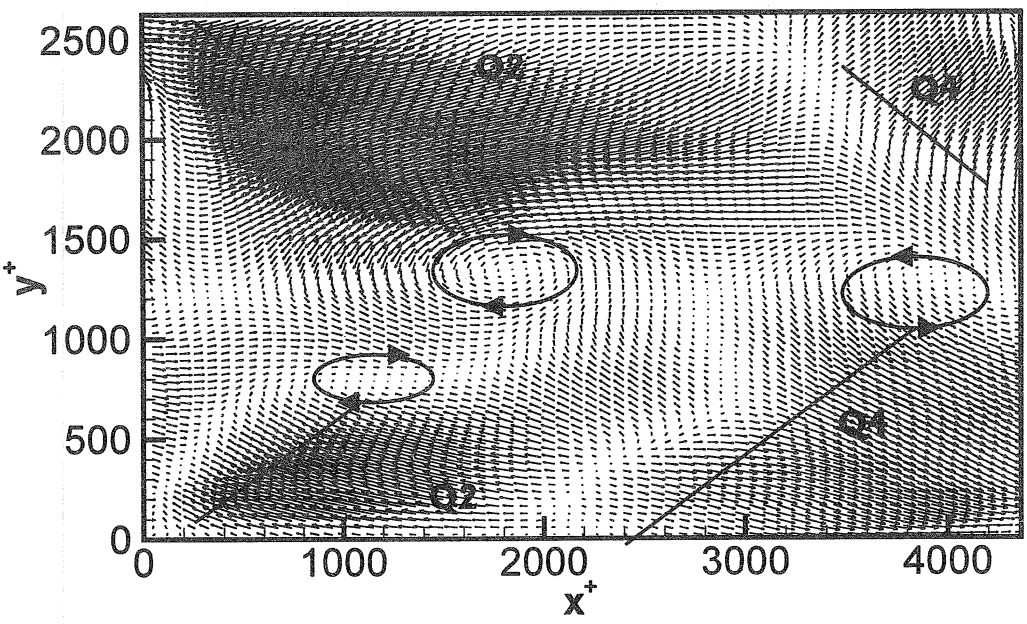
Q2
Q1
Q1
Q2
2500
2000
1500
1000
500
0
y+
0
1000
2000
3000
4000
x+

(b)

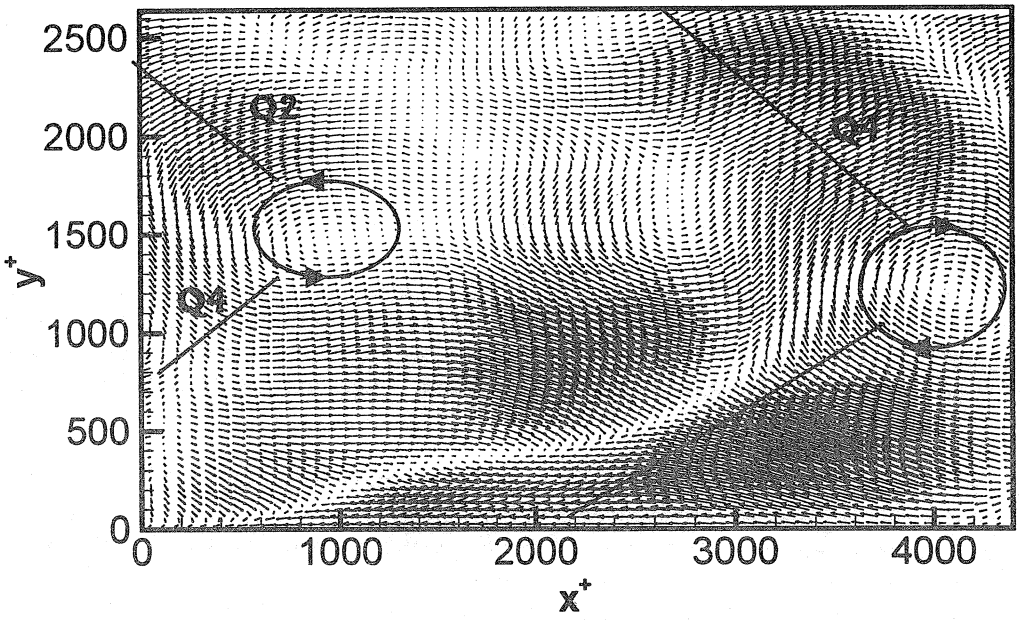

(c)

Figure 10. (a) An instantaneous turbulent fluctuating velocity field from PIV measurements at Re_h = 29,935; (b) The projection onto the first 12 eigenmodes (k = 0 - 2, n = 1 - 4). (c) The projection of another flow field onto the same first 12 eigenmodes (k = 0 - 2, n = 1 - 4).

Table 5: The phases, $\alpha^{(k,n)}$, and amplitudes, $|a^{(k,n)}|$, of the weighting coefficients, $a^{(k,n)}$, used in the projections of the two instantaneous realizations on to 12 eigenmodes for the two Reynolds numbers. The square roots of the corresponding eigenvalues are listed for a comparison.

Order	Re_h = 5,378			Re_h = 29,935		
(k, n)	$\alpha^{(k,n)}$	$\lvert a^{(k,n)}\rvert$	$\sqrt{\lambda^{(k,n)}}$	$\alpha^{(k,n)}$	$\lvert a^{(k,n)}\rvert$	$\sqrt{\lambda^{(k,n)}}$
(0, 1)	0.0	0.271	0.522	0.0	2.430	0.621
(0, 2)	0.0	0.280	0.482	0.0	1.820	0.504
(0, 3)	0.0	0.450	0.273	0.0	1.210	0.269
(0, 4)	0.0	0.453	0.262	0.0	1.860	0.232
(1, 1)	-0.973	0.414	0.370	-0.240	0.466	0.404
(1, 2)	-0.123	0.102	0.368	-1.320	2.880	0.369
(1, 3)	-0.641	0.244	0.303	-1.240	1.150	0.303
(1, 4)	-0.853	0.284	0.248	-0.567	0.692	0.250
(2, 1)	-0.423	0.216	0.249	1.170	0.775	0.238
(2, 2)	-1.320	0.079	0.211	0.914	0.566	0.226
(2, 3)	0.913	0.145	0.183	0.618	0.574	0.191
(2, 4)	0.651	0.122	0.175	-1.050	0.098	0.162

that the eddies have random spanwise locations relative to the fixed plane of the PIV data the high frequency with which the signatures are observed indicates that these structures are indeed characteristic of the large scale fields.

5. Conclusions

Turbulent flow fields in the outer region of flow through a rectangular channel at Re_h = 5,378, and Re_h = 29,935 have been measured in the streamwise-wall-normal plane and analyzed by two-dimensional proper orthogonal decomposition. The scaling of the outer flow structures was found to be only approximately the same for the two Reynolds numbers. The measurements at the larger Reynolds number reveal a slightly larger contribution from smaller scale motions. This can be seen by comparing the eigenmodes in Tables 3 and 4 and the correlation functions in Figs. 1 and 2.

There are two principle results. *First*, the low order eigenmodes that carry much of the turbulent kinetic energy are large-scale motions having wavelengths equal to or longer than 3.2h. *Second*, these large-scale motions also carry most of the Reynolds stress. The six eigenmodes, (0 - 2, 1 - 2), carry 33% of the energy and 56% of the Reynolds shear stress at Re_h = 5,378; they carry 37% of the energy and 50% of the Reynolds shear stress at Re_h = 29,935. The inclusion of 6 additional modes [(2, 1), (1, 3), (2, 2), (1, 4), (2, 4), (0, 4)] captures 48% and 50% of the energy for the two Reynolds numbers, respectively, and 67%and 75% of the respective Reynolds shear stresses. At low Reynolds number there is little difference between the large and small structures, and the fact that the first few modes carry much of the Reynolds stress is not surprising. For example, in the flow studied by Moin & Moser (1989) h^+ = 180, and the small-scale motions having length of order 100 viscous units are of the same size as those spanning the channel. At Reynolds number of 5,378 and most especially at 29,935 the large scales truly are much larger than the small scales, e.g. h^+ = 1,414. Hence, the low modes are very large, and it is surprising that they carry so much Reynolds stress. That the large-scale motions are highly active in the transport of streamwise momentum implies that the Reynolds stresses are far from being a local phenomenon, which has significant ramifications regarding the modeling of the Reynolds shear stress using Boussinesq eddy viscosity or other gradient transport models. It is interesting to note that a discussion of the possibility of large-scale motions constituting an important transport mechanism can be found in Hinze (1975).

At both Reynolds numbers the energy associated with the normal velocity is carried by motions that are significantly smaller than the scale of the largest streamwise motions. For example at the higher Reynolds number the streamwise motions extend 2 - 4h, while the largest wall-normal motions extend 0.3h. Since the Reynolds shear stress is also carried by the large-scale u-component flows, this implies that the v-component of the flows associated with Reynolds shear stress is not very energetic. It is difficult to imagine a turbulent motion whose u-component extends over a region much longer that that of the v-component. One such motion is the vortex packet discussed by Adrian *et al.* (1988, 1999). It consists of long regions of coherently aligned hairpin-like eddies. The largest of the individual eddies reach a significant fraction of the layer thickness, about 0.3h, and the length of the packets reaches 2 -4h. Within a packet, the individual eddies coherently induce a region of negative streamwise momentum, which, because of their coherent alignment, becomes a negative u-fluctuation almost as long as the packet. The induced flow is nearly parallel to the wall, i.e. it has little v-energy. Thus, within an individual eddy the u- and v-components may have similar scale, but the assembly of them has a much longer scale. The short v-correlation is associated with individual eddies; while the long u-correlation is associated with the coherent induction of many aligned eddies.

A comparison of the eigenmodes with actually observed flow fields shows that individual modes do not represent eddy structures. Their contributions to the flow field are best seen by projecting instantaneous realizations of the flow on to the eigenmodes. By doing this for the first twelve modes that contain one-half of the kinetic energy, it is found that large structures have a signature in the x-y plane that has been identified herein as the signature of a characteristic Reynolds stress event. These projected patterns have sizes on the order of the channel height.

This work was supported by ONR N00014-99-1-0188, NSF ATM95-22662, and NSF CTS 92-00936.

REFERENCES

Adrian, R. J. Particle-imaging techniques for experimental fluid mechanics. 1991 *Annu. Rev. Fluid Mech.* **23**, 261-304.

Adrian, R. J. & Lekakis I. C. 1991 A scale gap in the structure of moderate Reynolds number turbulent pipe flow. *Bull. Amer. Phys. Soc.,* Fluid Dynamics, **36**, 2698.

Adrian, R. J., Balachandar, S. & Tomkins, C. D. 1998 The Structure of Vortex Packets in Wall Turbulence. *AIAA 98-2962.*

Adrian, R. J., Meinhart, C. D. & Tomkins, C. D. 1999 Organization of vortical structure in the outer region of a the turbulent boundary layer. Submitted to *J. Fluid Mech.* Also, *TAM Report* No. 924, University of Illinois.

Bakewell, H. P. and Lumley, J. L. 1967 Viscous sublayer and adjacent wall region in turbulent pipe flow. *Phys. Fluids* **10**, 1880-1889.

Chambers, D. H., Adrian, R. J., Moin, P., Stewart, D. S., and Sung, H.J. 1988 Karhunen-Loève expansion of Burger's model of turbulence. *Phys. Fluid* **31**, 2573-2582.

Guenther, A., Papavassiliou, D.V., Warholic, M. D. & Hanratty, T. J. 1998 Turbulent flow in a channel at low Reynolds numbers. *Exp. Fluids* **25**, 503-511.

Grant, H. L. 1958 The large eddies of turbulent motion. *J. Fluid Mech.* **4**,149-190.

Hanratty, T. J., Adrian, R. J., Liu, Z. -C., Brook, J., Papavassiliou, D., McLaughlin J. 1993 Recent results on the structure of wall turbulence. In *Proc. Ninth Symp. Turbulent Shear Flows"*, Kyoto, 11.3.1-11.3.3.

Hinze, J. 1975 *Turbulence,* 2nd Ed. McGraw-Hill, New York, p. 579.

Herzog, S. 1986 *The large-scale structure in the near-wall region of turbulent pipe flow.* PhD thesis. Cornell University.

Kline, S. J., Reynolds, W. C. Schraub, F. A. & Runstadler, P. W. 1967 The structure of turbulent boundary layers. . *J. Fluid Mech.* **30**, part 4, 741-773.

Kovasznay, L. S. G., Kibens, V. & Blackwelder, R. F. 1970 Large-scale motion in the intermittent region of a turbulent boundary layer. *J. Fluid Mech.* **41**, 283-325.

Lee, M. J. and Kim, J. 1991 The structure of turbulence in a simulated plane Couette flow. In *Proc. Turbulent Shear Flow Symp.*, Munich, Sept. 9-11, 5.3.1-5.3.6.

Lekakis, I. C. 1988 *Coherent Structure in Turbulent Pipe Flow.* PhD Thesis, University of Illinois at Urbana-Champaign.

Liu, Z. -C, Landreth, C. C., Adrian, R. J., Hanratty, T. J. 1991 High resolution measurement of turbulent structure in a channel with particle image velocimetry. *Exp. Fluids* **10**, 301-312.

Liu, Z. -C, Adrian, R. J., Hanratty, T. J. 1994 Reynolds-number similarity of orthogonal decomposition of the outer layer of turbulent wall flow. *Phys. Fluids* **6**, 2815-2819.

Liu, Z. -C, Adrian, R. J., Hanratty, T. J. 1995 A study of turbulent channel flow with 2-D Proper Orthogonal Decomposition. *Bull. Amer. Phys. Soc.*, Fluid Dynamics, **40**, 2014.

Lu, J. L. & Smith, C. R. 1991 Velocity profile reconstruction using orthogonal decomposition. *Exp. Fluids* **11**, 247-254.

Lumley, J. L. 1970 *Stochastic Tools in Turbulence*. Academic, New York.

Moin, P. & Moser, R. D. 1989 Characteristic-eddy decomposition of turbulence in a channel. *J. Fluid Mech.* **200**, 471-509.

Moser, R. D. 1994 Kolmogorov inertial range spectra for inhomogeneous turbulence. *Phys. Fluids* **6**, 794-801.

Murlis, J., Tsai, H. M. & Bradshaw, P. 1982 The structure of turbulent boundary layers at low Reynolds numbers. *J. Fluid Mech.* **122**, 13-56.

Naguib, A. M. & Wark, C. E. 1992 An investigation of wall-layer dynamics using a combined temporal filtering and correlation technique. *J. Fluid Mech.* **243**, 541-560.

Naguib, A. M. & Wark, C. E. 1999 Personal communication.

Niederschulte, M. A., Adrian, R. J. & and Hanratty T. J. 1990 Measurements of turbulent flow in a channel at low Reynolds numbers. *Exp. Fluids* **9**, 222-230.

Papavassiliou, D. V. and Hanratty, T. J. 1997 Interpretation of large-scale structures observed in a turbulent plane Couette flow. *Int. J. Heat and Fluid Flow* **18**, 55-69.

Robinson, S. K. 1991 *The Kinematics of Turbulent Boundary Layer Structure*. NASA TM-103859.

Sirovich, L., Ball, K. S. & Keefe, L. R. 1990 Plane waves and structures in turbulent channel flow. *Phys. Fluids*, **A2** 2217-2226.

Sirovich, L., Ball, K. S. & Handler, R. A. 1991 Propagating structures in wall-bounded turbulent flows. *Theoret.Comput.Fluid Dynamics* **2**, 307-317.

Sung, H. J. & Adrian, R. J. 1994 Karhunen-Loève expansion of the derivative of an inhomogeneous process. *Phys. Fluids* **6**, 2233-2235.

Townsend, A. A. 1958 The turbulent boundary layer, in *Boundary Layer Research. Proc. IUTAM Symposium,* Freiburg, August 26-29, 1957, Springer-Verlag, Berlin. 1-15.

Townsend, A. A. 1976 *The Structure of Turbulent Shear Flow*, 2nd ed. Cambridge Univ. Press, Cambridge.

Warholic M. D. 1997 *Modification of Turbulent Channel Flow by Passive and Additive Devices,* PhD. Thesis, Univ. of Illinois at Urbana-Champaign.

Wygnanski, I. J. & Champagne, F. H. 1973 On transition in a pipe. Part 1. The origin of puffs and slugs and the flow in a turbulent slug. *J. Fluid Mech.* **59**, 281-335.

Appendix:

Figures of cross-correlations for the two Reynolds numbers

(c1)

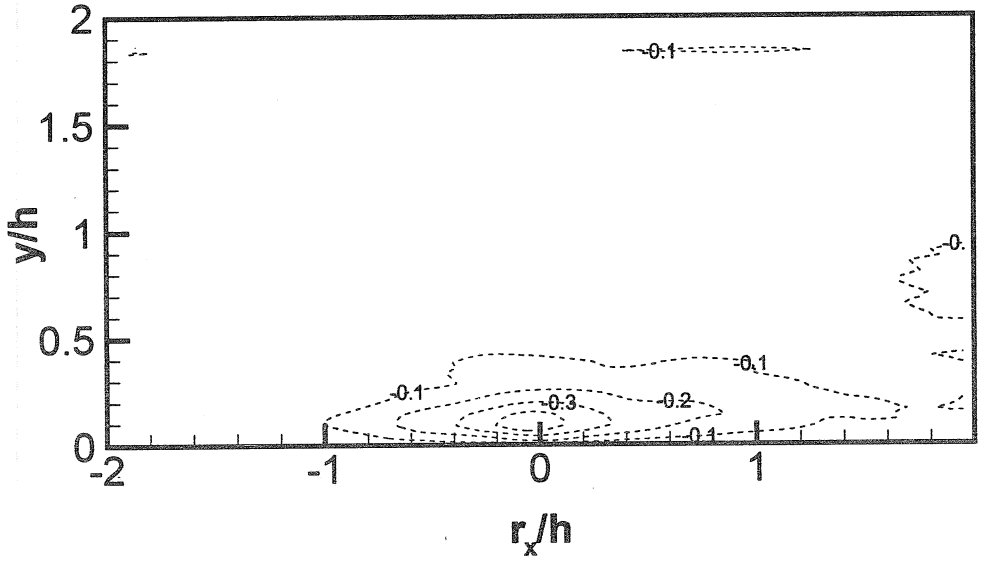
2
1.5
1
0.5
0
y/h
-2
-1
0
1
r_x/h
0.1
0.1
0.3
0.2
0.1
0.1
0.

(c2)

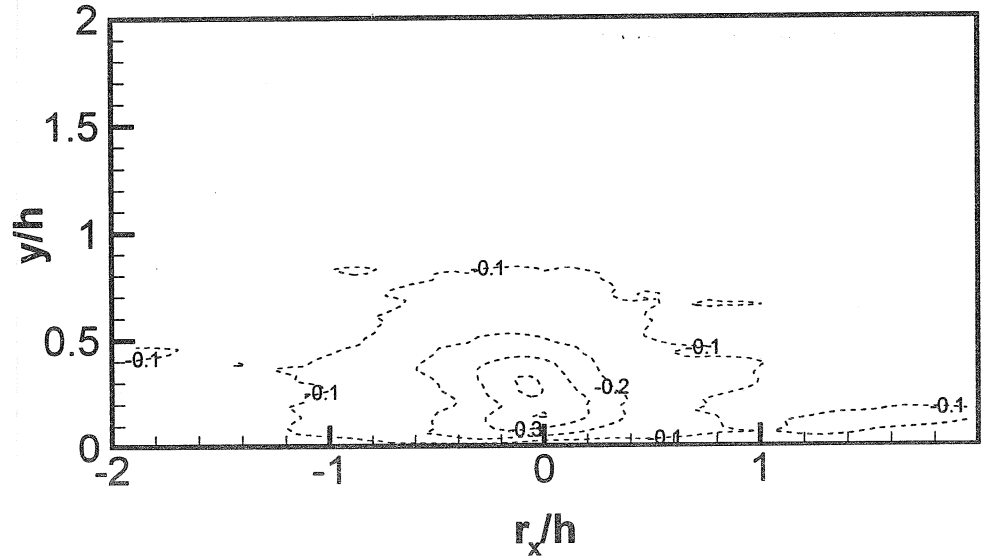
2
1.5
1
0.5
0
y/h
-2
-1
0
1
r_x/h
0.1
0.1
0.1
0.2
0.3
0.1
0.1

(c3)

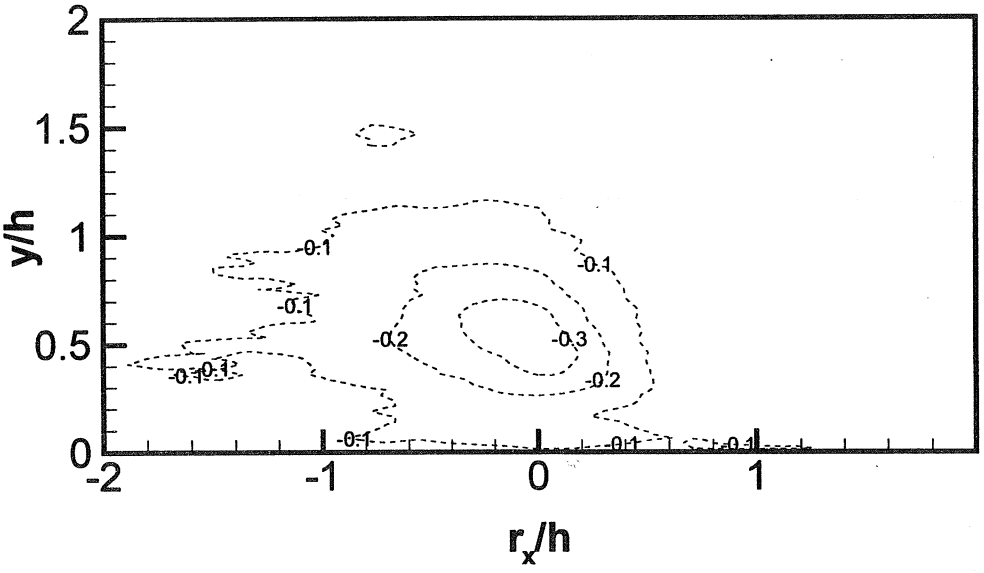

(c4)

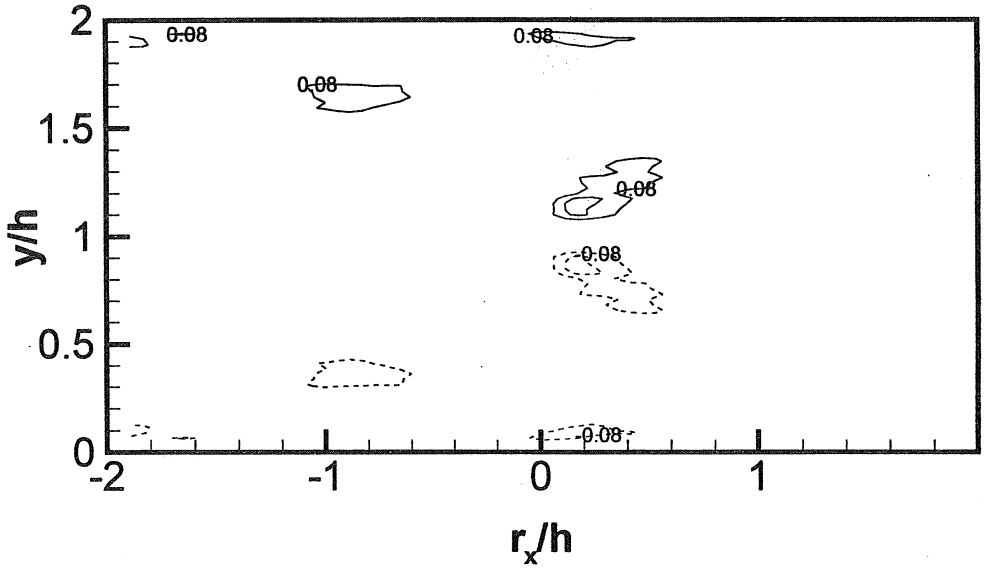

Figure 1A. Contours of the two-point cross-correlation coefficients for Re_h = 5,378. (c1) - (c4), $R_{uv}(r_x,y,y')/\sigma_u(y)\sigma_v(y')$; (b1) - (b4), $R_{vu}(r_x,y,y')/\sigma_v(y)\sigma_u(y')$. The locations of the fixed correlating points are: (a1) - (b1), y/h = 0.065 (y^+ = 20.5); (a2) - (b2), y/h = 0.237 (y^+ = 75); (a3) - (b3), y/h = 0.508 (or y^+= 160); (a4) - (b4), y/h = 1.0 (or y^+ = 315).

(d1)

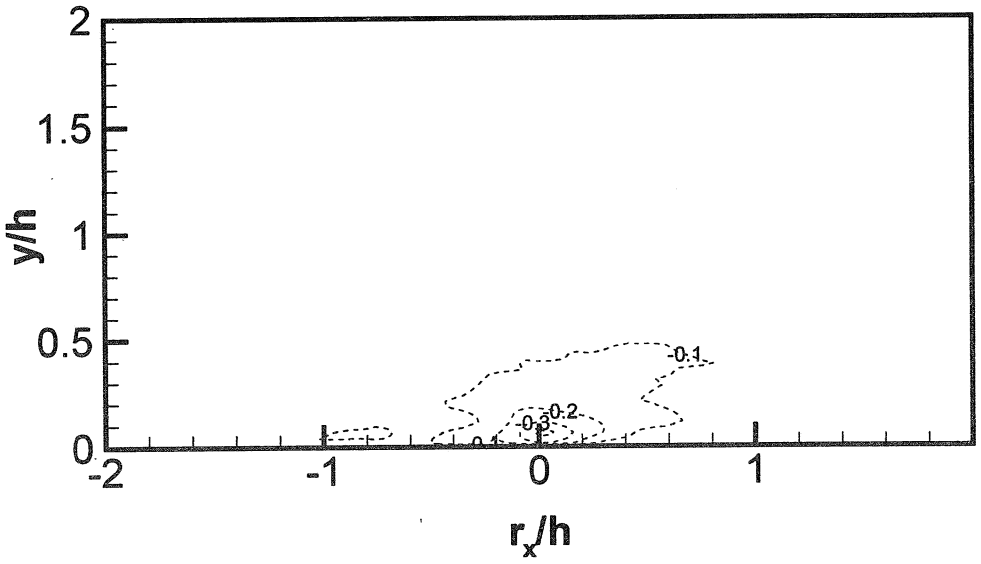

(d2)

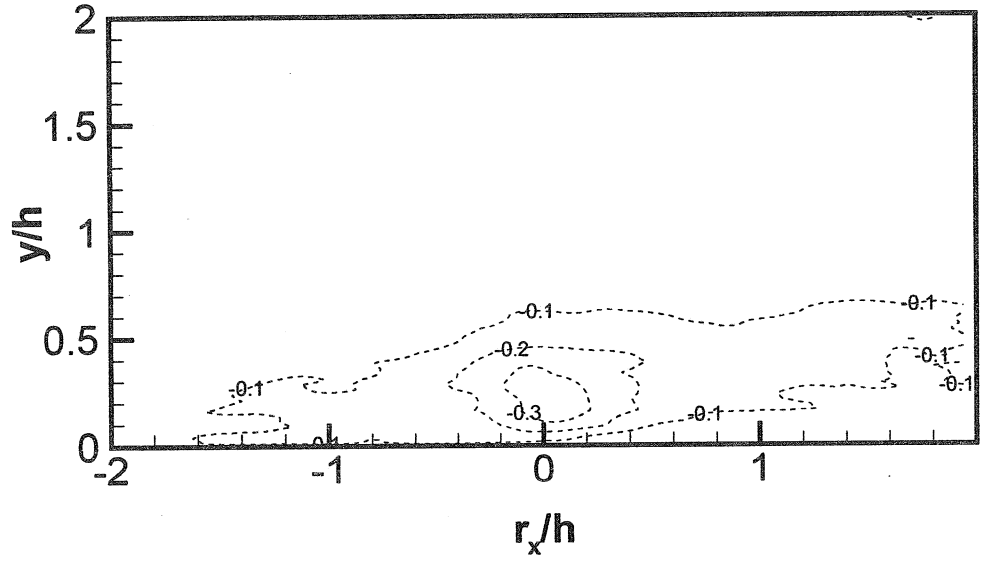

(d3)

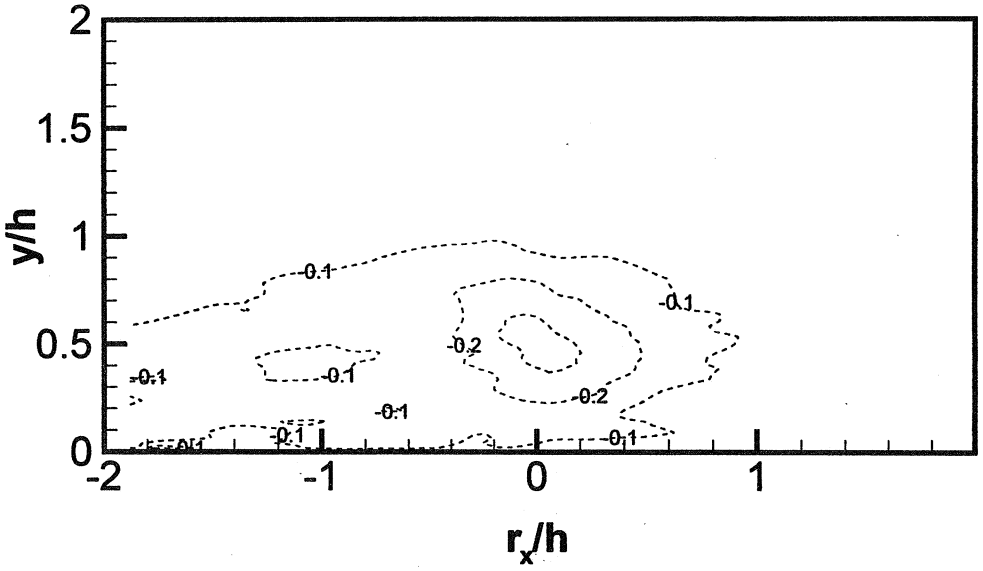

(d4)

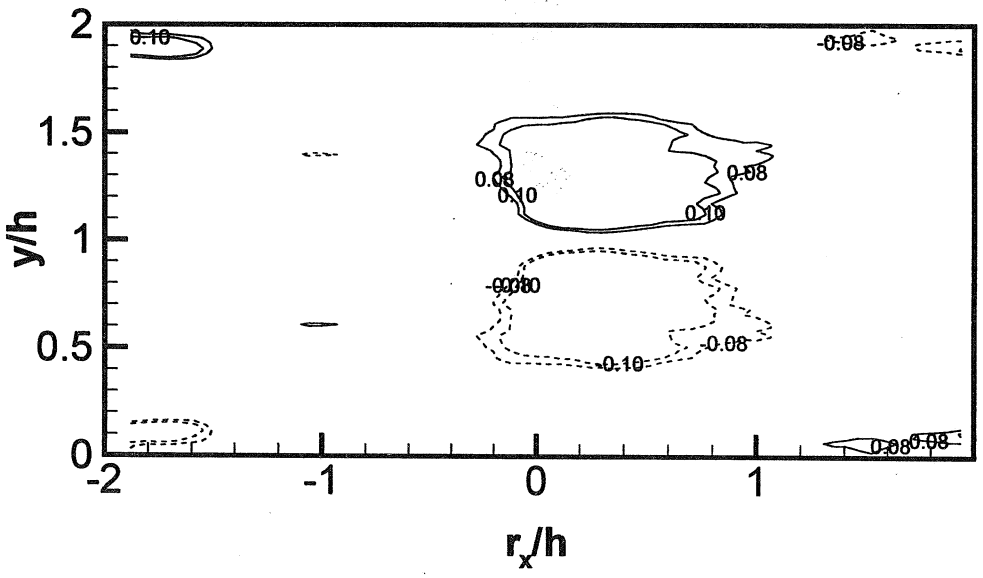

Figure 2A. Contours of the two-point correlation coefficients for Re_h = 29,935. (d1) - (d4), $R_{uv}(r_x,y,y')/\sigma_u(y)\sigma_v(y')$; (b1) - (b4), $R_{vu}(r_x,y,y')/\sigma_v(y)\sigma_u(y')$. The locations of the fixed correlating points are the same as in Fig. 2A.

List of Recent TAM Reports (cont'd)

No.	Authors	Title	Date
862	Short, M., and D. S. Stewart	Cellular detonation stability, I: A normal-mode linear analysis—*Journal of Fluid Mechanics* **368**, 229–262 (1998)	Sept. 1997
863	Carranza, F. L., and R. B. Haber	A numerical study of intergranular fracture and oxygen embrittlement in an elastic–viscoplastic solid—*Journal of the Mechanics and Physics of Solids*, **47**, 27–58 (1997)	Oct. 1997
864	Sakakibara, J., and R. J. Adrian	Whole-field measurement of temperature in water using two-color laser-induced fluorescence—*Experiments in Fluids* **26**, 7–15 (1999)	Oct. 1997
865	Riahi, D. N.	Effect of surface corrugation on convection in a three-dimensional finite box of fluid-saturated porous material—*Theoretical and Computational Fluid Dynamics*, 13, 189-208 (1999)	Oct. 1997
866	Baker, C. F., and D. N. Riahi	Three-dimensional flow instabilities during alloy solidification—*Bulletin of the American Physical Society* **41**, 1699 (1998)	Oct. 1997
867	Fried, E.	Introduction (only) to *The Physical and Mathematical Foundations of the Continuum Theory of Evolving Phase Interfaces* (book containing 14 seminal papers dedicated to Morton E. Gurtin), Berlin: Springer-Verlag, in press (1998)	Oct. 1997
868	Folguera, A., and J. G. Harris	Coupled Rayleigh surface waves in a slowly varying elastic waveguide—*Proceedings of the Royal Society of London A* **455**, 917–931 (1998)	Oct. 1997
869	Stewart, D. S.	Detonation shock dynamics: Application for precision cutting of metal with detonation waves	Oct. 1997
870	Shrotriya, P., and N. R. Sottos	Creep and relaxation behavior of woven glass/epoxy substrates for multilayer circuit board applications—*Polymer Composites* **19**, 567–578 (1998)	Nov. 1997
871	Riahi, D. N.	Boundary wave–vortex interaction in channel flow at high Reynolds numbers, *Fluid Dynamics Research* **25**, 129–145 (1999)	Nov. 1997
872	George, W. K., L. Castillo, and M. Wosnik	A theory for turbulent pipe and channel flows—paper presented at *Disquisitiones Mechanicae* (Urbana, Ill., October 1996)	Nov. 1997
873	Aslam, T. D., and D. S. Stewart	Detonation shock dynamics and comparisons with direct numerical simulation—*Combustion Theory and Modeling* **3**, 77–101 (1999)	Dec. 1997
874	Short, M., and A. K. Kapila	Blow-up in semilinear parabolic equations with weak diffusion *Combustion Theory and Modeling* **2**, 283-291 (1998)	Dec. 1997
875	Riahi, D. N.	Analysis and modeling for a turbulent convective plume—*Mathematical and Computer Modeling* **28**, 57–63 (1998)	Jan. 1998
876	Stremler, M. A., and H. Aref	Motion of three point vortices in a periodic parallelogram—*Journal of Fluid Mechanics* **392**, 101-128 (1999)	Feb. 1998
877	Dey, N., K. J. Hsia, and D. F. Socie	On the stress dependence of high-temperature static fatigue life of ceramics	Feb. 1998
878	Brown, E. N., and N. R. Sottos	Thermoelastic properties of plain weave composites for multilayer circuit board applications	Feb. 1998
879	Riahi, D. N.	On the effect of a corrugated boundary on convective motion—*Journal of Theoretical and Applied Mechanics*, in press (1999)	Feb. 1998
880	Riahi, D. N.	On a turbulent boundary layer flow over a moving wavy wall	Mar. 1998
881	Riahi, D. N.	Vortex formation and stability analysis for shear flows over combined spatially and temporally structured walls—*Mathematical Problems in Engineering* **5**, 317–328 (1999)	June 1998
882	Short, M., and D. S. Stewart	The multi-dimensional stability of weak heat release detonations—*Journal of Fluid Mechanics* **382**, 109–135 (1999)	June 1998
883	Fried, E., and M. E. Gurtin	Coherent solid-state phase transitions with atomic diffusion: A thermomechanical treatment—*Journal of Statistical Physics* **95**, 1361–1427 (1999)	June 1998
884	Langford, J. A., and R. D. Moser	Optimal large-eddy simulation formulations for isotropic turbulence—*Journal of Fluid Mechanics* **398**, 321–346 (1999)	July 1998

List of Recent TAM Reports

No.	*Authors*	*Title*	*Date*
840	Phillips, W. R. C.	On finite-amplitude rotational waves in viscous shear flows—*Studies in Applied Mathematics* **100**, in press (1998)	Jan. 1997
841	Riahi, D. N.	Direct resonance analysis and modeling for a turbulent boundary layer over a corrugated surface—*Acta Mechanica* **131**, 225–233 (1998)	Jan. 1997
842	Liu, Z.-C., R. J. Adrian, C. D. Meinhart, and W. Lai	Structure of a turbulent boundary layer using a stereoscopic, large format video-PIV—*Developments in Laser Techniques and Fluid Mechanics*, 259–273 (1997)	Jan. 1997
843	Fang, B., F. L. Carranza, and R. B. Haber	An adaptive discontinuous Galerkin method for viscoplastic analysis—*Computer Methods in Applied Mechanics and Engineering* **150**, 191–198 (1997)	Jan. 1997
844	Xu, S., T. D. Aslam, and D. S. Stewart	High-resolution numerical simulation of ideal and non-ideal compressible reacting flows with embedded internal boundaries—*Combustion Theory and Modeling* **1**, 113–142 (1997)	Jan. 1997
845	Zhou, J., C. D. Meinhart, S. Balachandar, and R. J. Adrian	Formation of coherent hairpin packets in wall turbulence—In *Self-Sustaining Mechanisms in Wall Turbulence*, R. L. Panton, ed. Southampton, UK: Computational Mechanics Publications, 109–134 (1997)	Feb. 1997
846	Lufrano, J. M., P. Sofronis, and H. K. Birnbaum	Elastoplastically accommodated hydride formation and embrittlement—*Journal of Mechanics and Physics of Solids*, **46**, 1497–1520 (1998)	Feb. 1997
847	Keane, R. D., N. Fujisawa, and R. J. Adrian	Unsteady non-penetrative thermal convection from non-uniform surfaces—In *Geophysical and Astrophysical Convection*, R. Kerr, ed. (1997)	Feb. 1997
848	Aref, H., and M. Brøns	On stagnation points and streamline topology in vortex flows—*Journal of Fluid Mechanics* **370**, 1–27 (1998)	Mar. 1997
849	Asghar, S., T. Hayat, and J. G. Harris	Diffraction by a slit in an infinite porous barrier—*Wave Motion*, **30**, 96–104 (1998)	Mar. 1997
850	Shawki, T. G., H. Aref, and J. W. Phillips	Mechanics on the Web—Proceedings of the International Conference on Engineering Education (Aug. 1997, Chicago)	Apr. 1997
851	Stewart, D. S., and J. Yao	The normal detonation shock velocity–curvature relationship for materials with non-ideal equation of state and multiple turning points—*Combustion* **113**, 224–235 (1998)	Apr. 1997
852	Fried, E., A. Q. Shen, and S. T. Thoroddsen	Wave patterns in a thin layer of sand within a rotating horizontal cylinder—*Physics of Fluids* **10**, 10–12 (1998)	Apr. 1997
853	Boyland, P. L., H. Aref, and M. A. Stremler	Topological fluid mechanics of stirring—*Bulletin of the American Physical Society* **41**, 1683 (1996)	Apr. 1997
854	Parker, S. J., and S. Balachandar	Viscous and inviscid instabilities of flow along a streamwise corner—*Bulletin of the American Physical Society* **42**, 2155 (1997)	May 1997
855	Soloff, S. M., R. J. Adrian, and Z.-C. Liu	Distortion compensation for generalized stereoscopic particle image velocimetry—*Measurement Science and Technology* **8**, 1–14 (1997)	May 1997
856	Zhou, Z., R. J. Adrian, S. Balachandar, and T. M. Kendall	Mechanisms for generating coherent packets of hairpin vortices in near-wall turbulence—*Bulletin of the American Physical Society* **42**, 2243 (1997)	June 1997
857	Neishtadt, A. I., D. L. Vainshtein, and A. A. Vasiliev	Chaotic advection in a cubic stokes flow—*Physica D* **111**, 227 (1997).	June 1997
858	Weaver, R. L.	Ultrasonics in an aluminum foam—*Ultrasonics* **36**, 435–442 (1998)	July 1997
859	Riahi, D. N.	High gravity convection in a mushy layer during alloy solidification—In *Nonlinear Instability, Chaos and Turbulence*, D. N. Riahi and L. Debnath, eds., **1**, 301–336 (1998)	July 1997
860	Najjar, F. M., and S. Balachandar	Low-frequency unsteadiness in the wake of a normal plate, *Bulletin of the American Physical Society* **42**, 2212 (1997)	Aug. 1997
861	Short, M.	A parabolic linear evolution equation for cellular detonation instability—*Combustion Theory and Modeling* **1**, 313–346 (1997)	Aug. 1997

List of Recent TAM Reports (cont'd)

No.	Authors	Title	Date
907	Subramanian, S. J., and P. Sofronis	Modeling of the interaction between densification mechanisms in powder compaction	May 1999
908	Aref, H., and M. A. Stremler	Four-vortex motion with zero total circulation and impulse—*Physics of Fluids* **11,** 3704-3715	May 1999
909	Adrian, R. J., K. T. Christensen, and Z.-C. Liu	On the analysis and interpretation of turbulent velocity fields—*Experiments in Fluids,* in press (1999)	May 1999
910	Fried, E., and S. Sellers	Theory for atomic diffusion on fixed and deformable crystal lattices	June 1999
911	Sofronis, P., and N. Aravas	Hydrogen induced shear localization of the plastic flow in metals and alloys	June 1999
912	Anderson, D. R., D. E. Carlson, and E. Fried	A continuum-mechanical theory for nematic elastomers	June 1999
913	Riahi, D. N.	High Rayleigh number convection in a rotating melt during alloy solidification	July 1999
914	Riahi, D. N.	Buoyancy driven flow in a rotating low Prandtl number melt during alloy solidification	July 1999
915	Adrian, R. J.	On the physical space equation for large-eddy simulation of inhomogeneous turbulence	July 1999
916	Riahi, D. N.	Wave and vortex generation and interaction in turbulent channel flow between wavy boundaries	July 1999
917	Boyland, P. L., M. A. Stremler, and H. Aref	Topological fluid mechanics of point vortex motions	July 1999
918	Riahi, D. N.	Effects of a vertical magnetic field on chimney convection in a mushy layer	Aug. 1999
919	Riahi, D. N.	Boundary mode–vortex interaction in turbulent channel flow over a non-wavy rough wall	Sept. 1999
920	Block, G. I., J. G. Harris, and T. Hayat	Measurement models for ultrasonic nondestructive evaluation	Sept. 1999
921	Zhang, S., and K. J. Hsia	Modeling the fracture of a sandwich structure due to cavitation in a ductile adhesive layer	Sept. 1999
922	Nimmagadda, P. B. R., and P. Sofronis	Leading order asymptotics at sharp fiber corners in creeping-matrix composite materials	Oct. 1999
923	Yoo, S., and D. N. Riahi	Effects of a moving wavy boundary on channel flow instabilities	Nov. 1999
924	Adrian, R. J., C. D. Meinhart, and C. D. Tomkins	Vortex organization in the outer region of the turbulent boundary layer	Nov. 1999
925	Riahi, D. N., and A. T. Hsui	Finite amplitude thermal convection with variable gravity	Dec. 1999
926	Kwok, W. Y., R. D. Moser, and J. Jiménez	A critical evaluation of the resolution properties of *B*-spline and compact finite difference methods	Feb. 2000
927	Ferry, J. P., and S. Balachandar	A fast Eulerian method for two-phase flow	Feb. 2000
928	Thoroddsen, S. T., and K. Takehara	The coalescence–cascade of a drop	Feb. 2000
929	Liu, Z.-C., R. J. Adrian, and T. J. Hanratty	Large-scale modes of turbulent channel flow: Transport and structure	Feb. 2000

List of Recent TAM Reports (cont'd)

No.	Authors	Title	Date
885	Riahi, D. N.	Boundary-layer theory of magnetohydrodynamic turbulent convection—*Proceedings of the Indian National Academy (Physical Science)* **65A**, 109–116 (1999)	Aug. 1998
886	Riahi, D. N.	Nonlinear thermal instability in spherical shells—in *Nonlinear Instability, Chaos and Turbulence* **2**, in press (1999)	Aug. 1998
887	Riahi, D. N.	Effects of rotation on fully non-axisymmetric chimney convection during alloy solidification—*Journal of Crystal Growth* **204**, 382–394 (1999)	Sept. 1998
888	Fried, E., and S. Sellers	The Debye theory of rotary diffusion	Sept. 1998
889	Short, M., A. K. Kapila, and J. J. Quirk	The hydrodynamic mechanisms of pulsating detonation wave instability—*Proceedings of the Royal Society of London, A* **357**, 3621–3638 (1999)	Sept. 1998
890	Stewart, D. S.	The shock dynamics of multidimensional condensed and gas phase detonations—Proceedings of the 27th International Symposium on Combustion (Boulder, Colo.)	Sept. 1998
891	Kim, K. C., and R. J. Adrian	Very large-scale motion in the outer layer—*Physics of Fluids* **2**, 417–422 (1999)	Oct. 1998
892	Fujisawa, N., and R. J. Adrian	Three-dimensional temperature measurement in turbulent thermal convection by extended range scanning liquid crystal thermometry—*Journal of Visualization* **1**, 355-364 (1999)	Oct. 1998
893	Shen, A. Q., E. Fried, and S. T. Thoroddsen	Is segregation-by-particle-type a generic mechanism underlying finger formation at fronts of flowing granular media?—*Particulate Science and Technology* **17**, 141–148 (1999)	Oct. 1998
894	Shen, A. Q.	Mathematical and analog modeling of lava dome growth	Oct. 1998
895	Buckmaster, J. D., and M. Short	Cellular instabilities, sub-limit structures, and edge-flames in premixed counterflows—*Combustion Theory and Modeling* **3**, 199–214 (1999)	Oct. 1998
896	Harris, J. G.	*Elastic waves*—Part of a book to be published by Cambridge University Press	Dec. 1998
897	Paris, A. J., and G. A. Costello	Cord composite cylindrical shells	Dec. 1998
898	Students in TAM 293–294	Thirty-fourth student symposium on engineering mechanics (May 1997), J. W. Phillips, coordinator: Selected senior projects by M. R. Bracki, A. K. Davis, J. A. (Myers) Hommema, and P. D. Pattillo	Dec. 1998
899	Taha, A., and P. Sofronis	A micromechanics approach to the study of hydrogen transport and embrittlement	Jan. 1999
900	Ferney, B. D., and K. J. Hsia	The influence of multiple slip systems on the brittle–ductile transition in silicon—*Materials Science Engineering A* **272**, 422–430 (1999)	Feb. 1999
901	Fried, E., and A. Q. Shen	Supplemental relations at a phase interface across which the velocity and temperature jump	Mar. 1999
902	Paris, A. J., and G. A. Costello	Cord composite cylindrical shells: Multiple layers of cords at various angles to the shell axis	Apr. 1999
903	Ferney, B. D., M. R. DeVary, K. J. Hsia, and A. Needleman	Oscillatory crack growth in glass—*Scripta Materialia* **41**, 275–281 (1999)	Apr. 1999
904	Fried, E., and S. Sellers	Microforces and the theory of solute transport	Apr. 1999
905	Balachandar, S., J. D. Buckmaster, and M. Short	The generation of axial vorticity in solid-propellant rocket-motor flows	May 1999
906	Aref, H., and D. L. Vainchtein	The equation of state of a foam	May 1999